1

Nanchangmycin regulates FYN, FAK and ERK to control the fibrotic activity
of hepatic stellate cells

4

Wenyang Li[1,2], Jennifer Y. Chen[1,2], Cheng Sun[1,2], Robert P. Sparks[1,2], Lorena Pantano[3],

Raza-Ur Rahman[1,2], Sean P. Moran[1,2], Joshua V. Pondick[1,2], Rory Kirchner[3], David Wrobel[2],

Michael Bieler[5], Shannan J. Ho Sui[3], Julia F. Doerner[5], Jörg F. Rippmann[5], Alan C.

Mullen[1,2,4*]

9

1. Gastrointestinal Unit, Massachusetts General Hospital, Boston, MA, USA

2. Harvard Medical School, Boston, MA, USA

3. Harvard T.H. Chan School of Public Health, Boston, MA, USA

4. Harvard Stem Cell Institute, Cambridge, MA, USA

5. Boehringer Ingelheim Pharma GmbH & Co. KG, Biberach a.d. Riss, Germany

15

* Corresponding author. Thier 306B, 55 Fruit Street, Massachusetts General Hospital,

Boston, MA 02114, USA. Email: acmullen@mgh.harvard.edu

18

Current Addresses:

20

Wenyang Li: College of Chemistry and Molecular Engineering, Peking University, Beijing,

100871, China

23

Jennifer Y. Chen: Department of Medicine, University of California, San Francisco, San

Francisco, CA 94115, USA; Liver Center, Department of Medicine, University of California,

San Francisco, San Francisco, CA 94143, USA

27

28

29   **Abstract**

30

31   Chronic liver injury causes fibrosis, characterized by the formation of scar tissue resulting from

32   excessive accumulation of extracellular matrix (ECM) proteins. Hepatic stellate cell (HSC)

33   myofibroblasts are the primary cell type responsible for liver fibrosis, yet there are currently no

34   therapies directed at inhibiting the activity of HSC myofibroblasts. To search for potential anti-

35   fibrotic drugs, we performed a high-throughput compound screen in primary human HSC

36   myofibroblasts and identified 19 small molecules that induce HSC inactivation, including the

37   polyether ionophore nanchangmycin (NCMC). NCMC induces lipid re-accumulation while

38   reducing collagen expression, deposition of collagen in the extracellular matrix, cell

39   proliferation, and migration. We find that NCMC increases cytosolic Ca^{2+} and reduces the

40   phosphorylated protein levels of FYN, FAK, ERK1/2, HSP27 and STAT5B. Further, depletion

41   of each of these kinases suppress *COL1A1* expression. These studies reveal a signaling

42   network triggered by NCMC to inactivate HSC myofibroblasts and reduce expression of

43   proteins that compose the fibrotic scar. The identification of the antifibrotic effects of NCMC

44   and the pathways by which NCMC inhibits fibrosis provides new tools and therapeutic targets

45   to combat the development and progression of liver fibrosis.

46

Introduction

Chronic liver disease and cirrhosis are the 11th leading cause of mortality in the United States, accounting for over 40,000 deaths annually (Murphy et al., 2021). Liver injuries, including those caused by viral infection, excessive alcohol intake, and nonalcoholic steatohepatitis can lead to fibrosis, the accumulation of abnormal scar tissue, in the liver (Bataller & Brenner, 2005). If left unchecked, liver fibrosis can progress to cirrhosis and end-stage liver disease (Bataller & Brenner, 2005). HSC myofibroblasts are the primary cell type responsible for liver fibrosis (Friedman et al., 1985; Mederacke et al., 2013). HSCs reside in the perisinusoidal space and represent 5-8% of total cells in the liver. In their quiescent, nonfibrotic state, they store vitamin A as retinol ester in lipid droplets (Geerts, 2001). In response to chronic liver injury, HSCs are activated and trans-differentiate into HSC myofibroblasts, characterized by the loss of lipid droplets, increased contractility, and secretion of ECM proteins, leading to fibrosis (Bataller & Brenner, 2005; Friedman, 2008).

Resolution of liver fibrosis has been observed when the source of liver injury is removed, such as in patients with successful antiviral therapy against hepatitis B or C (Benyon & Iredale, 2000; Bonis et al., 2001; Falize et al., 2006). Two mechanisms can contribute to the reduction of activated HSC myofibroblasts during resolution of liver fibrosis – apoptosis of activated HSC myofibroblasts and reversion of HSC myofibroblasts to a more quiescent phenotype (Friedman, 2008). With regression of fibrosis, 40-50% of HSC myofibroblasts revert to an inactive state *in vivo,* which is associated with reduced collagen expression (Kisseleva et al., 2012; Troeger et al., 2012). These encouraging observations suggest that liver fibrosis is reversible and targeting HSC myofibroblasts to induce an inactive phenotype may serve as a therapeutic approach to treat patients with liver fibrosis.

Despite many efforts to understand HSC plasticity and target HSC myofibroblasts, there are currently no FDA-approved therapies directed at inhibiting the activity of HSC myofibroblasts.

75   In our previous studies, we developed a novel small molecule screen to identify compounds

76   that promote HSC inactivation (Chen et al., 2017). In a pilot screen, this approach revealed

77   the antifibrotic effects of tricyclic antidepressants (TCAs). In mechanistic studies, we identified

78   that TCAs inhibit the enzyme acid ceramidase (aCDase). In subsequent studies, we

79   demonstrated that inhibiting aCDase regulates YAP/TAZ-mediated HSC inactivation and

80   reduces fibrogenesis in mouse models and in human precision cut liver slices (Alsamman et

81   al., 2020).

82

83   Here, we expanded our screen approximately ten-fold to include 15,867 experimental wells

84   and developed a secondary screen to evaluate primary hits. We find that nanchangmycin

85   (NCMC), a polyether ionophore, promotes HSC inactivation. Furthermore, we demonstrate

86   that NCMC decreases proliferation, migration, and assembly of collagen fibers in the

87   extracellular matrix. In additional mechanistic studies, we show that multiple kinases and

88   signaling pathways are involved in mediating the impact of NCMC on HSC activities, including

89   the FYN, FAK and ERK pathways. Taken together, this study defines NCMC as a potent

90   antifibrotic compound that inactivates HSC myofibroblasts and highlights the FYN, FAK and

91   ERK pathways as potential downstream targets to inhibit liver fibrosis.

92

93   **Results**

94

95   *A high-throughput small molecule screen identifies compounds that inactivate human hepatic*

96   *stellate cell myofibroblasts*

97

98   To identify small molecules that induce reversion of HSC myofibroblasts to an inactive

99   phenotype, we screened 24 compound libraries consisting of 15,867 experimental wells using

100 a high-throughput method to quantify lipid droplet accumulation as an indicator of HSC

101 inactivation (Chen et al., 2017) (Figure 1A, Supplementary Table 1, and Supplementary Table

102 2). Activated HSCs were seeded in 384-well plates, treated with compounds for 48 hours,

4

103   fixed, and stained with Bodipy, a fluorescent lipid dye, to analyze the accumulation of lipid

104   droplets as a marker of HSC inactivation. DMSO and nortriptyline were included as negative

105   and positive controls, respectively on each plate. A scaled value was calculated for each

106   experimental well based on the average percentage of Bodipy-positive cells, toxicity, and

107   reproducibility and was normalized according to negative and positive controls on the same

108   plate to minimize plate-specific effects.

109

110   Experimental wells with a scaled value higher than 0.85, a cutoff set as the top 10th percentile

111   of nortriptyline-treated wells on the same plate, were defined as hits. To avoid losing potential

112   hits due to plate-specific effects, the top three experimental wells with the highest scaled

113   values on each plate were also included as hits even if their scaled values did not meet the

114   0.85 cutoff. A total of 711 experimental wells, containing 464 different compounds, met these

115   criteria and were identified as primary hits (Figure 1B and Supplementary Table 3).

116

117   To further narrow the candidate list for secondary screening, the 711 hits were separated into

118   102 clusters based on their chemical structure, with an average cluster size of seven

119   compounds. The highest scoring hit with the most common structure within each cluster was

120   selected as the representative compound for the cluster. Among the 102 representative

121   compounds, ten compounds were removed because they contained pan assay interference

122   structures (Baell & Nissink, 2018) or were themselves frequently identified as hits in screens.

123   One compound was removed because it was a TCA, and we have previously demonstrated

124   that TCAs target the sphingolipid pathway to inhibit HSC activity (Chen et al., 2017). One

125   additional compound was removed because it had the same molecular formula as another

126   selected hit (Supplementary Table 4). In addition to representative compounds selected from

127   each cluster, 50 compounds with high scaled values or promising structures were also

128   selected. In total, 140 unique compounds were included in the secondary screen (Figure 1A

129   and Supplementary Table 5).

130

131   *Development of a secondary screening assay in primary human HSCs*

132

133   Activated HSCs are characterized by increased expression of α-SMA (encoded by *ACTA2*)

134   and type 1 collagen (encoded by *COL1A1*) (Bataller & Brenner, 2005; Friedman, 2008). We

135   developed a high-throughput secondary assay to quantify *ACTA2* and *COL1A1* mRNA levels

136   as indicators of HSC activity. HSCs were treated with compounds for 48 hours and then lysed

137   for multiplexed qRT-PCR to quantify the house-keeping reference mRNA in the same well as

138   *ACTA2* or *COL1A1*. Since a proper reference mRNA is critical for qRT-PCR based assays,

139   we evaluated 18 housekeeping genes, consisting of seven commonly used genes as well as

140   eleven reference genes identified from the literature (Eisenberg & Levanon, 2013). We first

141   analyzed RNA sequencing data from HSCs under multiple conditions (Chen et al., 2017).

142   Among these candidates, *GUSB*, *POLR2A*, *EMC7*, *VCP*, *PSMB2* and *VPS29* showed the

143   lowest standard deviation (0.15 or less). Further comparison of expression of these genes in

144   inactivated HSCs (induced by the addition of nortriptyline or ceramide (Chen et al., 2017)) and

145   culture-activated HSCs revealed that *GUSB*, *POLR2A*, *EMC7* and *PSMB2* had the least fold

146   change in expression (10% or less upon HSC inactivation). Thus, we selected these four

147   reference mRNAs for further evaluation. *GAPDH*, which is used routinely as a reference

148   control, was also included for comparison (Figure 1 – figure supplement 1A). We quantified

149   expression using qRT-PCR in HSC cDNA samples reverse-transcribed from equal amounts

150   of total RNA. *PSMB2*, which encodes proteasome 20S subunit beta 2, showed the least

151   variation as indicated by standard deviation and was chosen as the reference mRNA for the

152   secondary qRT-PCR-based screen (Figure 1 – figure supplement 1B).

153

154   qRT-PCR was performed to quantify *ACTA2, COL1A1* and *PSMB2* mRNA levels in each

155   sample. Relative fold changes were calculated compared to DMSO control. We defined the

156   following as criteria for compound advancement: 1. Fold change of *COL1A1* was reduced to

157   less than 0.5 of DMSO control (FDR<0.05); 2. Fold change of *ACTA2* was reduced to less

158   than 0.5 of DMSO (FDR<0.05); 3. Averaged *PSMB2* expression was between 0.2-2.0 of

159 DMSO (Figure 1C and Supplementary Table 5). This last criterion was added to avoid

160 selecting compounds where large changes in *PSMB2* expression made it difficult to interpret

161 changes in *ACTA2* and *COL1A1* expression. Of the 140 compounds, a total of 44 compounds

162 met all three criteria. Five compounds were not commercially available, and 39 compounds

163 were advanced for further analysis.

164

165 Next, we evaluated dose response curves (DRCs) for each compound at eight different

166 concentrations, from 10 pM to 10 µM, using a Bodipy lipid accumulation assay similar to that

167 employed in the primary screen. Dose response curves were scored blindly by three

168 researchers (Supplementary Table 6 and Methods), and nortriptyline served as a reference.

169 Of the 39 compounds, 19 received an average score that was the same as or higher than

170 nortriptyline controls (Figure 1D, Figure 1 – figure supplement 2, and Table 1).

171

172 Nine compounds had a DRC score less than 2 and an EC50 less than 5 µM and were

173 considered the highest priority. Two subgroups of compounds were identified within this group

174 based on similar bioactivity – histone deacetylase inhibitors (HDACIs), including trichostatin A

175 and abexinostat, and Na/K-ATPase inhibitors, including ouabain, digitoxigenin, and digoxin.

176 Histone deacetylases are linked to a variety of fibrotic disorders, including liver fibrosis (Pang

177 & Zhuang, 2010). HDACIs, such as MC1568 and Valproate, have been reported to reduce

178 HSC activation and alleviate liver fibrosis in animal models (Yoon et al., 2019). The presence

179 of HDACIs in our final candidate list supports the validity of our screening approach in

180 identifying potential liver fibrosis inhibitors. Na/K-ATPase activity may play a role in non-

181 alcoholic fatty liver disease (Sodhi et al., 2017), but it is not clear how Na/K-ATPases regulate

182 HSC activity and liver fibrosis. Due to the toxicity and narrow therapeutic dose range of cardiac

183 glycosides, which limit their potential application in treatment of liver fibrosis, we decided not

184 to pursue further evaluation of this group of compounds. Nanchangmycin (NCMC), a natural

185 product of *Streptomyces nanchangensis*, is a polyether insecticidal antibiotic (Sun et al., 2002)

186 and is one of the most potent hits. Studies of NCMC are limited, but it has been shown to have

187   a broad spectrum of antiviral activity against diverse arboviruses (Rausch et al., 2017) and

188   potentially SARS-CoV-2 infection (Dittmar et al., 2020; Li et al., 2020; Svenningsen et al.,

189   2020). It also suppresses breast cancer stem cell activity and inhibits growth of breast cancer

190   and multiple myeloma cells (Huang et al., 2018; Xu et al., 2020). The cellular targets of NCMC

191   remain largely unknown, and its effect on HSC activation and liver fibrosis has not been

192   investigated. Therefore, we selected this compound to further validate its function in regulating

193   HSC activity and explore its mechanism of action.

194

195   *Nanchangmycin induces lipid accumulation in both human and mouse primary HSCs*

196

197   First, we confirmed the effect of NCMC on lipid accumulation in primary HSCs isolated from

198   four human donors of different age, gender and race (donor information provided in Materials

199   and Methods). We observed that NCMC treatment significantly increased lipid droplet

200   accumulation in primary HSC lines compared to controls (Figure 2A), consistent with HSC

201   inactivation. Compared to nortriptyline (Chen et al., 2017), NCMC exhibited higher potency in

202   HSCs from all four donors, where 100-300 nM of NCMC exhibited similar effects on lipid

203   droplet accumulation to 10 µM nortriptyline (Figure 2B and Figure 2 – figure supplement 1).

204   As we switched to NCMC from a different source with higher purity, we found that the new

205   NCMC stock has a lower EC50 in HSCs from human donors and HSCs from C57BL/6 mice

206   (Figure 2C-D and Figure 2 – figure supplement 2). These results show that NCMC induces

207   lipid accumulation in both human and murine HSCs.

208

209   *NCMC inhibits fibrotic gene expression in HSCs*

210

211   We next quantified the effect of NCMC on *ACTA2* and *COL1A1* expression in multiple primary

212   human HSC lines. NCMC treatment reduced both *ACTA2* and *COL1A1* levels at 100 nM or

213   higher (Figures 3A-B). We also observed a dose-dependent effect of NCMC on *Acta2* and

214   *Col1a1* expression in murine HSCs at day 2 (Figure 3C). To investigate how NCMC affects

8

215   the level of collagen deposited into the ECM, we performed the scar-in-a-jar assay to

216   accelerate the process of ECM deposition with addition of molecular crowding reagents and

217   TGF-β (Chen et al., 2009; Good et al., 2019). NCMC treatment significantly decreased

218   collagen staining intensity and fiber area (Figures 3D-E). In addition to two-dimensional (2D)

219   cell culture models, we also tested NCMC's effect on *COL1A1* expression in spheroids

220   consisting of primary human HSCs and primary rat hepatocytes. Both the basal expression of

221   *COL1A1* and TGF-β-induced *COL1A1* expression were significantly reduced by NCMC

222   treatment (Figure 3F).

223

224   HSCs were next treated with NCMC and analyzed by RNA-sequencing analysis, which

225   revealed that NCMC broadly affects genes associated with fibrosis. Among the top gene sets

226   negatively enriched in the NCMC-treated group were ECM-related signatures, including ECM

227   structural constituent and collagen-containing ECM, as well as signatures relevant to migration,

228   including contractile fibers. Of note, genes associated with oligosaccharide lipid intermediate

229   biosynthetic process were positively enriched, possibly contributing to the re-accumulation of

230   lipid droplets (Figure 3G and Supplementary Table 7). We compared the RNA sequencing

231   data with a canonical HSC gene signature (Zhang et al., 2016), an HSC-specific signature that

232   is highly and uniquely expressed in HSCs and correlates with the extent of fibrosis (Zhang et

233   al., 2016), and the liver cirrhosis signature from Disgenet database (Piñero et al., 2020). We

234   observed that these signatures were significantly negatively enriched (Figure 3 – figure

235   supplement 1 and Supplementary Table 8). Visualization of the canonical HSC gene signature

236   (Zhang et al., 2016) also demonstrated that many genes that promote liver fibrosis, including

237   those that encode collagens, TGF-β, and PDGF pathway components, are inhibited by NCMC

238   (Figure 3H and Supplementary Table 8). Taken together, these data suggest that NCMC

239   triggers a global change in HSC gene expression, resulting in a decrease in profibrotic activity.

240

241   *NCMC reduces migration and proliferation of HSCs*

242

243   In addition to secretion of ECM proteins, activated HSCs demonstrate enhanced migration

244   capabilities (Hernandez-Gea & Friedman, 2011). Thus, we performed transwell migration and

245   scratch wound healing assays to evaluate how NCMC affects HSC migration. HSCs were pre-

246   treated with NCMC for two days before seeding in cell culture inserts with permeable

247   membranes. After 6-24 hours, HSCs that migrated through the membrane were stained and

248   counted. NCMC treatment significantly reduced the number of cells that migrated through the

249   membrane compared to DMSO controls (Figure 4A).

250

251   We also examined the wound healing capability of HSCs. HSCs were seeded onto plates

252   containing inserts that block cells from accessing and attaching to a strip at the bottom of the

253   well. After removal of the insert, DMSO or 1 µM NCMC was added, and HSCs filled the gap

254   or "wound" field through migration and proliferation. After 30 hours of treatment, the DMSO-

255   treated control cells closed the gap, whereas the gap remained for NCMC-treated cells (Figure

256   4B). While inhibition of HSC migration by NCMC is likely the major contributor to the difference

257   observed between NCMC treatment and controls at shorter time points, such as 6 hours for

258   the transwell assay, the difference at longer time points could be attributed to reductions in

259   both migration and proliferation.

260

261   We next determined how NCMC affects HSC proliferation. We treated HSCs isolated from two

262   human donors with DMSO control and increasing concentrations of NCMC and counted

263   Hoechst-stained nuclei on five consecutive days. NCMC treatment reduced cell proliferation

264   at concentrations of 25 nM and higher, and this effect on proliferation was first evident on day

265   2 (Figure 4C). A fraction of HSCs undergo apoptosis with the removal of fibrotic stimuli *in vivo*

266   (Kisseleva et al., 2012), and we evaluated the contribution of apoptosis to the effect of NCMC

267   on day 2. Based on the analysis of Annexin V and propidium iodide (PI) by flow cytometry,

268   NCMC treatment only showed a small increase in the percentage of apoptotic cells in one of

269   two donor HSC lines at 1 µM and no increase at 100nM. There was also a small increase in

270   necrotic cells in NCMC treatment compared to controls (Figure 4D). In addition, analysis of

271 the proliferation marker Ki-67 and PI showed that NCMC treatment increased the percentage

272 of G0 quiescent cells (Figure 4E and Figure 4 – figure supplement 1). Taken together, these

273 results suggest that HSCs enter a more quiescent-like, non-proliferative state upon NCMC

274 treatment, and apoptosis was only observed in a small fraction of cells.

275

276 *Modulation of Ca^{2+} signaling may contribute to the effect of NCMC on HSC inactivation*

277

278 NCMC is a polyether ionophore and has been shown to increase cytosolic Ca^{2+} in a cancer

279 cell line (Huang et al., 2018). We examined the activity of NCMC as a calcium ionophore in

280 HSCs. We loaded HSCs with a fluorescent Ca^{2+} indicator (Fluo-4 NW) and treated cells with

281 NCMC. Ionomycin and thapsigargin were included as positive controls (Jones & Sharpe, 1994;

282 Morgan & Jacob, 1994). At 10 µM, NCMC increased cytosolic Ca^{2+} as did ionomycin and

283 thapsigargin (Figure 4F). We also performed the same analysis with ethylene glycol tetraacetic

284 acid (EGTA) to chelate Ca^{2+} and eliminate any contribution from extracellular Ca^{2+} during the

285 assay. Similar to the effect observed with thapsigargin (Ribeiro et al., 2018), the increase of

286 cytosolic Ca^{2+} in response to NCMC was not sensitive to EGTA (Figure 4 – figure supplement

287 2A), suggesting that the immediate increase of cytosolic Ca^{2+} following NCMC treatment is

288 due to release of calcium from intracellular stores. Analysis of a dose response of NCMC

289 demonstrated an increase in cytosolic Ca^{2+} at concentrations as low as 10 nM (Figure 4G and

290 Figure 4 - figure supplement 2B).

291

292 *NCMC reduces COL1A1 expression in HSCs through the FYN pathway*

293

294 Calcium signaling regulates mitogen-activated protein kinases and non-receptor tyrosine

295 kinases (Filvaroff et al., 1990; Rusanescu et al., 1995; Xia et al., 1996), and we analyzed a

296 kinase array to define kinase signaling molecules modulated by NCMC. HSCs were treated

297 with DMSO or 1 µM NCMC for 1 and 18 hours (Figure 5A). Among the 45 proteins tested,

298 FYN phosphorylation at Y420 was reduced by approximately 40% at both 1 hour and 18 hours.

11

299   We selected HSP27 (HSPB1), ERK1/2 (MAPK3/1), STAT5A/B, and FAK (PTK2) to study

300   further in addition to FYN because 1) they also showed decreased phosphorylation at 18 hours,

301   and 2) genes encoding these products are expressed at a relatively high level in HSCs, as

302   indicated from RNA sequencing data, suggesting that these may also be potential mechanistic

303   targets of NCMC in HSCs.

304

305   To further investigate the role of these seven kinases in human HSCs, we depleted each

306   kinase using pooled siRNAs in human HSCs from three donors. We observed a consistent

307   reduction of *COL1A1* with depletion of *FYN*, *HSP27*, *ERK1*, *ERK2* and *STAT5B* (Figures 5B-

308   C, Figure 5 – figure supplement 1), suggesting that each kinase contributes to regulation of

309   *COL1A1* expression.

310

311   Among the kinases that consistently reduced *COL1A1* expression, the reduction of FYN

312   phosphorylation at Y420 was the most prominent following one hour of NCMC treatment,

313   indicating that FYN may mediate the immediate response to NCMC in HSCs. Therefore, we

314   further investigated FYN activity. Western blot of FYN revealed two bands -- the upper band

315   was reduced in HSCs treated with NCMC, while the lower band showed little change (Figure

316   6 – figure supplement 1A). Both bands were reduced with depletion of FYN (Figure 6 – figure

317   supplement 2), suggesting that both products are encoded by *FYN* mRNA. FYN

318   phosphorylation was not directly evaluated because antibodies that uniquely recognize

319   phosphorylated FYN are not available. We also probed with a phospho-Src family antibody,

320   which recognizes phosphorylated FYN and other Src family proteins (Figure 6 – figure

321   supplement 1B). Two bands of approximately the same size are observed with FYN antibody

322   and pSrc antibody, suggesting that both bands may represent phosphorylated FYN, while it is

323   the product in the upper band that is affected by NCMC treatment. qPCR analysis of NCMC-

324   treated HSCs showed that *FYN* mRNA level was not affected (Figure 6 – figure supplement

325   3), further indicating that NCMC regulates FYN through a post transcriptional mechanism.

326

327   Both depletion of FYN using two different siRNA duplexes (Figure 6A-B) and treatment with

328   1-Naphthyl PP1, an inhibitor of v-Src, FYN, and ABL (Figure 6C), significantly reduced

329   *COL1A1* mRNA level in HSCs. Collagen deposition in the ECM was also impaired by FYN

330   depletion, as indicated by the reduced collagen intensity and fiber area in the scar-in-a-jar

331   assay (Figures 6D). In addition, ectopic expression of a dominant negative Y213A FYN mutant

332   (Kaspar & Jaiswal, 2011) reduced *COL1A1* expression in HSCs but did not further decrease

333   *COL1A1* level in NCMC-treated cells, suggesting that FYN inhibition is likely to be downstream

334   of NCMC (Figure 6E). Lastly, expression of dominant negative FYN in HSCs resulted in a

335   decrease in phosphorylated ERK (Figure 6F), suggesting that FYN may crosstalk with the

336   ERK pathway to exert its function.

337

338   *ERK1/2 and FAK regulate HSC migration*

339

340   Next, we asked if FYN regulates other HSC phenotypes that are observed with NCMC

341   treatment. HSCs were transfected with pooled FYN siRNAs, and after 3 days, cells were

342   seeded for transwell migration assay. As FAK is known to regulate migration of lung fibroblasts

343   (Zhao et al., 2016) and HSCs (Zhao et al., 2017), we included FAK siRNAs as a positive

344   control. While FAK depletion consistently suppressed migration of HSCs isolated from three

345   different human donors, FYN depletion only reduced migration in one HSC line (Figure 7A-B).

346   We also observed that dominant negative FYN promotes phosphorylation of FAK (Figure 6F),

347   while NCMC reduces phosphorylation of FAK (Figure 6 – figure supplement 4), suggesting

348   that NCMC controls FAK phosphorylation and HSC migration through a pathway that is

349   independent of FYN.

350

351   We further tested how other kinases affected by NCMC (ERK1/2 and HSP27) regulate HSC

352   migration. Depletion of ERK1/2 consistently reduced migration across different donors,

353   whereas the influence of HSP27 depletion varied across HSCs from different donors (Figure

354   7C). These data indicate that NCMC regulates HSC migration through multiple downstream

355   signaling pathways likely targeting FAK and ERK1/2 as the primary paths to inhibit migration.

356

357   **Discussion**

358

359   Liver fibrosis is the major driver of liver failure in all etiologies of chronic liver disease, and the

360   degree of fibrosis is the strongest predictive factor for liver-related mortality (Anstee et al.,

361   2019). Current therapies for liver fibrosis focus on eliminating the underlying etiology. However,

362   there is a lack of effective treatment for several chronic liver diseases, such as non-alcoholic

363   fatty liver disease, which affects one in four people worldwide (Younossi et al., 2016), and

364   primary sclerosing cholangitis (Karlsen et al., 2017). Therefore, there is an urgent need to

365   develop antifibrotic therapies. Activation of HSCs in the setting of chronic liver injury

366   represents a critical event in fibrosis, as activated HSC myofibroblasts are the primary source

367   of collagen production and excessive extracellular matrix deposition (Friedman et al., 1985;

368   Maher & McGuire, 1990; Mederacke et al., 2013). With evidence that the scarring process in

369   the liver is reversible (Sun et al., 2020) and that HSC myofibroblasts demonstrate plasticity

370   and can revert to an inactive state (Kisseleva et al., 2012; Troeger et al., 2012), there is

371   increasing enthusiasm for development of approaches to promote HSC inactivation as a

372   therapeutic strategy to treat liver fibrosis. Although some therapies under investigation in

373   clinical trials, including PPAR agonists and TGF-β inhibitors, are anticipated to promote HSC

374   inactivation, none have yet been recognized as effective antifibrotic agents (Guo & Lu, 2020).

375

376   Therefore, with the goal to identify new antifibrotic compounds and novel pharmacological

377   targets for the treatment of liver fibrosis, we performed a small molecule compound screen

378   using primary human HSC myofibroblasts. Combining high-content microscopy imaging and

379   high-throughput qPCR screening approaches as well as filtering methods that take into

380   consideration both the potency and diversity of the candidates' chemical structures, we

381   screened 15,867 experimental wells and identified 19 candidates. Further studies to

382   investigate the compounds identified by the screen will deepen our understanding of HSC

383   biology and allow identification of additional genes and pathways that could be targeted to

384   reduce liver fibrosis.

385

386   We focused on NCMC because it strongly induced HSC inactivation, and the activity of NCMC

387   was poorly understood. NCMC belongs to a group of naturally occurring polyether ionophores,

388   which consist of over 120 known members (Huang et al., 2018). Among them, the compound

389   monensin shares a similar chemical structure to NCMC and is also a positive hit in our primary

390   screen. It was grouped in the same chemical cluster as NCMC, but NCMC was selected as

391   the representative compound for this cluster in the screen because NCMC had a higher scaled

392   value (Supplementary Table 4). This group of compounds demonstrates antibacterial,

393   antifungal, antiparasitic, antimalarial, antiviral, anti-inflammatory activities and cytotoxicity in

394   cancer cells (Kevin Ii et al., 2009). Although some polyether ionophores have been employed

395   as veterinary antibiotics, none have been used as antibiotics in human, possibly due to

396   concerns about toxicity (Huczyński, 2012). Indeed, we observe that NCMC demonstrated

397   substantial cytotoxicity in cell culture at concentrations higher than 10 μM (Figure 2 – figure

398   supplement 1). However, given that the EC50 of NCMC in lipid accumulation assay is in the

399   range of 10-300 nM without inducing apoptosis, NCMC or compounds with similar structure

400   may have potential as antifibrotic therapy within optimized therapeutic doses.

401

402   Despite the extensive study of some polyether ionophores, limited data are available

403   describing the activity and mechanism of action of NCMC in mammalian cells. A screen for

404   bioactive inhibitors of the Otub1/c-Maf axis in multiple myeloma cells demonstrated that NCMC

405   induces c-Maf polyubiquitination and proteasomal degradation in the presence of Otub1 (Xu

406   et al., 2020). A-130-A, a close analog of NCMC, also inhibited the Wnt/β-catenin pathway and

407   induced autophagy, and both A-130-A and NCMC increased cytosolic Ca^{2+} and reactive

408   oxygen species (ROS) as well as enhanced the permeability of the mitochondrial inner

409   membrane to H^+ and K^+ (Huang et al., 2018). To examine a wide variety of signaling pathways

410   that may be affected downstream of NCMC, we performed a phospho-kinase array analysis

411   to measure the phosphorylation of 37 kinases at a total of 43 different sites and the total protein

412   expression of β-catenin and HSP60. Seven kinases, including FYN, HSP27, ERK1, ERK2,

413   STAT5A, STAT5B, and FAK, were selected and further tested because their phosphorylated

414   protein was reduced by NCMC treatment, and all were relatively abundant in HSCs. When

415   depleted individually in HSCs from multiple donors, most of these kinases reduced *COL1A1*

416   level consistently (Figure 5B), suggesting that each may play a role in mediating NCMC's

417   effect on collagen expression. It is unclear why STAT5A siRNAs, which effectively depleted

418   *STAT5A* but also reduced *STAT5B* mRNA level, did not significantly affect *COL1A1*

419   expression, considering that reduction of *STAT5B* alone to a similar level by STAT5B siRNAs

420   did demonstrate an inhibitory effect (Figure 5B-C and Figure 5 – figure supplement 1). It is

421   possible that the expression of STAT5B protein is inhibited more efficiently in HSCs

422   transfected with STAT5B siRNAs than those transfected with STAT5A siRNAs despite the

423   similar mRNA levels. STAT5A/B homo- and hetero-dimers could have different individual

424   DNA-binding specificities (Maurer et al., 2019), and the ratio of homo- to hetero-dimers could

425   also affect transcription of the *COL1A1* gene.

426

427   Our investigations of FYN revealed that depletion or inhibition of FYN activity suppresses

428   collagen expression in primary human HSCs and deposition of collagen in the ECM, but

429   regulation via FYN did not explain all the effects observed with NCMC. The regulation of

430   collagen expression by FYN is in agreement with a recent study demonstrating that FYN

431   depletion and inhibition in the presence of TGF-β reduces collagen I expression in

432   immortalized human and rat HSC lines (Du et al., 2020). This study also observed that FYN

433   depletion and inhibition in the presence of TGF-β reduced HSC migration (Du et al., 2020),

434   however, our data did not show a consistent effect on migration with depletion of FYN. As cell

435   migration is controlled by a complex signaling network, the difference in the basal activity of

436   the signaling pathways up- or down-stream of FYN may account for the observed differences.

437   In contrast, FAK and ERK1/2 depletion showed a more robust and consistent inhibitory effect

438 among all HSC lines tested, suggesting that these kinases may serve as the critical nodes

439 regulating HSC migration. Depletion or inhibition of FYN or ERK suppresses HSC proliferation

440 (Du et al., 2020; Pagès et al., 1993), and FAK regulates proliferation in many cell types (Zhou

441 et al., 2019). Thus, it is likely that modulation of multiple kinases contributes to the anti-fibrotic

442 effect of NCMC, although the involvement of each kinase may vary depending on the cellular

443 context.

444

445 We found that NCMC increases cytosolic Ca^{2+}. Although it has not been demonstrated

446 experimentally, it is suspected that NCMC may increase cytosolic Ca^{2+} levels by disrupting

447 Na^+/Ca^{2+} exchange (Huang et al., 2018). Of note, the Na^+/K^+-ATPase inhibitors identified in

448 our screen can also increase cytosolic Ca^{2+} levels (Tian & Xie, 2008), and increased cytosolic

449 Ca^{2+} has been observed to inhibit ERK1/2 in fibroblasts (Bosch et al., 1998; Chuderland et al.,

450 2020; Cook et al., 1997). As a ubiquitous second messenger with wide-ranging physiological

451 roles, cytosolic Ca^{2+} levels may be a key factor mediating the downstream anti-fibrotic activity

452 of NCMC, but further investigations are needed to unravel the complete signaling cascade.

453

454 In summary, this study has identified NCMC as an antifibrotic compound that increases

455 cytosolic Ca^{2+} and regulates multiple kinases, including FYN, FAK and ERK1/2 to drive the

456 inactivation of HSC myofibroblasts (Figure 7C). Targeting an individual component of this

457 complex network may suppress certain cellular activities and contribute to HSC inactivation,

458 but it may be necessary to synergistically manipulate multiple targets to achieve antifibrotic

459 effects among the general population. By regulating multiple signaling pathways, NCMC

460 confers a more robust impact than observed with inhibition of only one pathway and thus could

461 represent a more effective strategy to halt fibrosis progression.

462

463 **Materials and Methods**

464

465 *Cell culture and compound*

466

467 Human primary hepatic stellate cells from donors 1, 2 and 5 were isolated from human

468 nonparenchymal liver cells (NPCs) purchased from Lonza (cat# HUCNP) as described

469 previously (Chen et al., 2017). Human primary hepatic stellate cells from donors 3 and 4 were

470 purchased as isolated hepatic stellate cells from Lonza (cat# HUCLS). Donor information is

471 listed below.

Donor	Lonza ID	Age	Gender	Race	BMI
1	4105	45	M	Caucasian	24.2
2	4270	35	M	Caucasian	42.1
3	180761	57	F	Caucasian	23.6
4	182821	24	F	African American	48.8
5	4258	51	M	African American	24.5

472

473 All hepatic stellate cells were cultured in Dulbecco's Modified Eagle Medium (DMEM) with 10%

474 fetal calf serum (FCS) and 1% Penicillin/Streptomycin (P/S). The primary lipid accumulation

475 screen and secondary mRNA screen were conducted with HSCs from donor 1 at passage 8,

476 the dose response curve screen was conducted with HSCs from donor 2 at passage 8 or 9,

477 and all other experiments were conducted with HSCs from donors as indicated at passage 8-

478 10.

479

480 Nanchangmycin (NCMC) was purchased from two sources. The initial confirmation of dose

481 response curves in multiple HSC lines (Figure 2B and Figure 2 – figure supplement 1) were

482 performed with NCMC purchased from Selleck Chemicals (cat# S1450). All other experiments

483 were performed with NCMC purchased from Adooq (cat# A10621) for higher purity. 1-

484 Naphthyl PP1 was purchased from Tocris (cat# 3063). Thapsigargin (Sigma-Aldrich, cat#

18

485 T9033) and ionomycin (Biogems, cat# 5608212) was purchased from Sigma. Stock solutions

486 were made with DMSO.

487

488 *Primary high-throughput lipid accumulation screen*

489

490 For each of the 5-day screening cycle, cells were plated on day 1 at 1000 cells/well in 30

491 µl/well of complete media in 384-well plates using Multidrop Combi (Thermo). On day 3, 100

492 nL/well of compounds from the libraries were transferred by a stainless-steel pin array and

493 Seiko compound transfer robot to the assay plates in duplicates. On day 5, the cells were fixed

494 with 4% paraformaldehyde (diluted with DPBS from 16% stock, Electron Microscopy Sciences,

495 cat# 15710) and incubated at room temperature for 15 min. The cells were washed one time

496 with DPBS and incubated with Bodipy 493/503 (0.25 µg/mL, Invitrogen, cat# D3922) and

497 Hoechst (5 µg/mL, Invitrogen, cat# H1399) for 45 min at room temperature. The plates were

498 washed three times with DPBS, and then 50 µl/well DPBS was added before sealing the plates

499 with adhesive foil cover. The plates were imaged using the ImageXpress Micro Confocal

500 (Molecular Devices) at the Institute of Chemistry and Cell Biology (ICCB)-Longwood screening

501 facility. Images of each well were analyzed using MetaXpress software to calculate the

502 percentage of positive cells (the total number of Bodipy positive cells (cutoff was adjusted for

503 each plate) divided by the total cell count).

504

505 We developed a scoring system to rank the strength of a compound in inducing HSC reversion

506 to the inactive phenotype. A score was calculated as follows: 1. Averaged percent positive

507 cells from duplicates was used to calculate the distance from the baseline of the plate

508 (percentile 75%), 2. Toxicity was penalized (the distance from the average number of cells in

509 the compound wells to the number of cells in the nortriptyline wells), and 3. Poor reproducibility

510 was penalized (the error of the two points to the average value of the duplicates). The score

511 was then normalized using nortriptyline and DMSO scores for each plate. A new parameter

19

512 was calculated termed "Scaled" with the formula: Scaled = -1*(median (nortriptyline)-

513 score)/abs(median (nortriptyline)-median(DMSO)) .

514

515 *Consolidation of screening library*

516

517 Chemical structures of the screening library were consolidated using the data science

518 workflow software BIOVIA Pipeline Pilot. Protonation states of the structures were

519 standardized, and counter ions were eliminated. We used canonical Simplified Molecular Input

520 Line Entry System (SMILES) as a unique linear textual representation of the chemical

521 structure. This way, the initial 15867 structures could be mapped onto 7696 unique canonical

522 SMILES of which 4329 are represented by a single well in the library and 3367 occur in up to

523 19 wells. Multiple occurrences of individual canonical SMILES could be traced to multiple

524 vendors and/or multiple molar concentrations of the individual probes. Using this analysis, the

525 711 experimental wells defined as hits were determined to represent 464 individual

526 compounds.

527

528 *Clustering analysis of primary screen candidates and selection for secondary analysis*

529

530 Hits were clustered into 102 groups of structurally similar compounds based on Tanimoto

531 similarities using the computational analysis software BIOVIA Pipeline Pilot. The distance to

532 the center of the cluster was calculated for each compound in the cluster using BIOVIA

533 Pipeline Pilot, and the most common structure for each cluster was defined based on this

534 value. The strongest hit with the most common structure for each cluster was selected as the

535 representative for the cluster. Promiscuous bioactive compounds that contain pan assay

536 interference structures (PAINS) (Baell & Nissink, 2018), or that we identified as frequent hits

537 in screens at ICCB-L were not included for further analysis, as the exhibited bioactivity may

538 be attributed to interference with specific assay readouts and/or nonspecific, intractable

539 mechanism of action (Matlock et al., 2018). Frequent hits were defined as having a positive

540   hit rate of more than 20% in screens performed at ICCB-L or more than 10 total positive hits

541   in the database of ICCB-L screens. One additional compound was removed because the

542   molecular formula was the same as another selected compound, and one compound was

543   removed due to similarity in structure to nortriptyline (Supplementary Table 4).

544

545   *Secondary mRNA screen for cherrypicked small molecules*

546

547   For each of the 5-day screening cycle, cells were plated in 384-well plates as in primary screen

548   on day 1. Compounds were added on day 3 using a digital non-contact dispenser D300e

549   (Hewlett Packard) in quadruplicate. On day 5, cell lysates for qPCR were prepared using the

550   Cells-to-C_T 1-Step Taqman Kit (Invitrogen, cat# A25603) according to manufacturer's

551   instructions. Briefly, cells were incubated with 25 µL/well lysis buffer (plus DNase) for 5

552   minutes at room temperature, and the reaction was stopped by adding 2.5 µL stop solution

553   and incubating for 2 minutes at room temperature. 2 µL cell lysates were used in the

554   multiplexed qRT-PCRs to measure *ACTA2*, *COL1A1*, and *PSMB2* mRNA levels. To reduce

555   technical variations, the TaqMan probe for endogenous control gene *PSMB2* was VIC-labeled

556   and primer-limited, so that the *PSBM2* probe can be multiplexed with FAM-labeled probe for

557   *ACTA2* or *COL1A1* in the same qRT-PCR. Details for probes are included in the "qPCR

558   analysis" section. The results were analyzed by fitting the data to the following linear models:

559   Ct_*ACTA2*~ Ct_*PSMB2* + plate + chemical or Ct_*COL1A1*~ Ct_*PSMB2* + plate + chemical.

560   Relative fold changes were calculated from the estimate of each chemical as compared to

561   DMSO control.

562

563   *Dose response curve screen*

564

565   The dose response curve screen was performed using an adapted lipid accumulation assay

566   with live human primary HSCs. Briefly, cells were plated at a density of 2500 cells/well in 384-

567   well plates. After 24 hours, compounds were added in duplicate at concentrations from 0.001

568   to 10 µM. Nortriptyline (10 µM) and DMSO (0.1%) served as controls. Cells were incubated

569   with compounds for 24 hours, followed by treatment with Bodipy (1 µg/ml; ThermoFisher, cat#

570   D3922) and NucLight Rapid Red (final dilution 1:4000; Essen BioSciences, cat# 4725) for an

571   additional 12 hours to stain lipid droplets and nuclei. Fluorescent signals were measured using

572   an Incucyte S3 system.

573

574   Bodipy stained area and nuclei count were determined selecting two fields per well. The

575   Bodipy-stained area per nuclei count was calculated per field and the mean was determined.

576   The percentage of lipid accumulation (referred to as % CTL) in response to compound

577   treatment was analyzed as follows: 100 x ((total green area/count [test compound] – total

578   green area/count [mean DMSO]) / (total green area/count [mean Nor] – total green area/count

579   [mean DMSO])). The total green area is a measure of lipid droplet accumulation in $µm^2$/well,

580   and count indicates the cell (nuclei) number per well.

581

582   The dose-response measurements were reviewed and scored independently by three

583   researchers based on the following criteria: Priority 1: the percentage of lipid accumulation (%

584   CTL) is increased at 1 µM, the shape suggests a sigmoidal distribution, and at least two

585   concentrations show increased Bodipy staining before the compound becomes toxic; Priority

586   2: compound treatment at 3.03 µM and 10 µM (highest concentrations) shows increased

587   Bodipy staining, and % CTL is at least 70% at 10 µM; Priority 3: compound treatment at 3.03

588   µM and 10 µM (highest concentrations) shows increased Bodipy staining, and % CTL is less

589   than 70% at 10 µM; Priority 4: only treatment at the highest concentration (10 µM) shows

590   increased Bodipy staining ; Priority 5: the curve is almost flat (no response).

591

592   *Estimation of EC50 for NCMC*

593

594   HSCs were plated in 384-well plates (Figure 2B) or 96-well plates (Figures 2C-D and Figure

595   2 – figure supplement 2), treated with NCMC at indicated concentrations for time points as

596   specified, and analyzed by lipid accumulation assay similar to the primary screen. Once the

597   percentage of Bodipy-positive cells was determined, the data were fitted into a sigmoidal four

598   parameter logistic model in Graphpad Prism software to estimate the EC50 of NCMC under

599   each condition.

600

601   *Fluorescent microscopy*

602

603   HSCs were seeded in black-wall 96-well plates (Corning, cat# 3603) and treated with NCMC

604   at different concentrations as indicated. After 48 hours, plates were fixed with 4%

605   paraformaldehyde and stained with Bodipy and Hoechst as in the primary lipid accumulation

606   screen. After the last wash, 200 µl/well DPBS was added, and plates were imaged using a

607   Nikon A1R confocal microscope.

608

609   *qPCR analysis*

610

611   qPCR analysis related to depletion of kinase candidates was performed using lysates

612   prepared with the Cells-to-C_T 1-Step Taqman Kit similar to the secondary mRNA screen,

613   except that HSCs were seeded in 96-well plates and 50 µl lysis buffer (with DNase) and 5 µl

614   stop solution were used. For the other qPCR analyses, RNA samples were prepared using

615   TRIzol (Invitrogen, cat# 15596026), and the concentrations were quantified using Qubit 3

616   fluorometer (Invitrogen) and the Qubit RNA BR Assay Kit (Invitrogen, cat# Q10211) according

617   to manufacturer's instructions. Reverse transcription was performed using iScript gDNA Clear

618   cDNA Synthesis Kit (BIO-RAD, cat# 1725035) with 1 µg total RNA input, and quantitative real-

619   time PCR was performed using TaqMan Universal PCR Master Mix (Applied Biosystems, cat#

620   4305719) and TaqMan Real-time PCR Assays for specific genes listed below.

Assay ID

23

Human *ACTA2*	Hs00426835_g1
Human *COL1A1*	Hs00164004_m1
Human *FYN*	Hs00176628_m1
Human *HSPB1/HSP27*	Hs00356629_g1
Human *MAPK1/ERK2*	Hs01046830_m1
Human *MAPK3/ERK1*	Hs00385075_m1
Human *PSMB2*	Hs01002946_m1
Human *PTK2/FAK*	Hs01056457_m1
Human *STAT5A*	Hs00559643_m1
Human *STAT5B*	Hs00560026_m1
Mouse *Acta2*	Mm00725412_s1
Mouse *Col1a1*	Mm00801666_g1
Mouse *Psmb2*	Mm00449477_m1

621

622   *Scar-in-a-jar (Siaj) assay*

623

624   To test the effect of NCMC on collagen deposition in ECM, HSCs were seeded in black-wall

625   96-well plates (Corning, cat# 3603) and treated with DMSO or 100 nM NCMC for 48 hours in

626   Ficoll medium, i.e. complete medium supplemented with 50 µg/ml L-ascorbic acid 2-

627   phosphate sesquimagnesium salt hydrate (Sigma, cat# A8960), 37.5 mg/ml Ficoll-PM70

628   (Sigma, cat# F2878), 25 mg/ml Ficoll-PM400 (Sigma, cat# F4375) and 5 ng/mL TGF-β (R&D

629   Systems, cat# 240-B-002). To test the effect of *FYN* depletion on collagen deposition, HSCs

24

630 were reverse transfected in 96-well plates with 50 nM non-targeting control siRNA or siRNAs

631 against *FYN* (see the "RNAi-mediated depletion of genes" section for specific information on

632 siRNAs and transfection reagents). After 48 hours, cells were incubated with Ficoll medium

633 for an additional 48 hours.

634

635 Cells were then fixed with ice-cold methanol for 2 min on ice, washed one time with DPBS and

636 then incubated with primary antibody against collagen type I in DPBS (1:1000, Sigma, cat#

637 C2456) at 4 ℃ overnight. After three washes with PBS-Tween (0.05% v/v), cells were

638 incubated with donkey anti-mouse Alexa Fluor 488 secondary antibody (1:500, Invitrogen,

639 cat# A-21202) and Hoechst (1:4000) in DPBS at room temperature for 1 hour. Plates were

640 washed three times with PBS-Tween, and after the final wash, 200 µL/well of DPBS was

641 added. Plates were imaged using the ImageXpress Micro Confocal microscope (Molecular

642 Devices) with 10x Plan Apo lens, and collagen fibers were analyzed using a custom module

643 built within the MetaXpress software.

644

645 *Liver spheroid experiment*

646

647 Liver spheroids were prepared as previously described (Leite et al., 2016) except spheroids

648 were formed from primary rat hepatocytes (Lonza, cat# RSCP01) and primary human HSCs.

649 Cells were seeded in ultra-low attachment round bottom 96-well plates (Greiner Bio-One, cat#

650 650970) at a ratio of 1:2. The cells were incubated in HCM hepatocyte culture media (Lonza,

651 cat# CC-3198) for one day with orbital shaking to allow the generation of liver spheroids. The

652 spheroids were then treated with DMSO or NCMC for 72 hours with or without TGF-β (5

653 ng/mL). Spheroids were collected, and RNA was extracted to quantify expression of human

654 *COL1A1* and *ACTA2* expression through qPCR.

655

656 *RNA sequencing*

657

658   HSCs were treated with DMSO or 1 µM NCMC for 48 hours. RNA was extracted using RNeasy

659   Mini kit (Qiagen, cat# 74104), followed by quality assessment via Agilent 2200 Tape Station.

660   Two biological samples were prepared for DMSO treatment and three biological samples were

661   prepared for NCMC treatment, and all samples had an RNA integrity number (RIN) greater

662   than 9. RNA library was prepared using TruSeq Stranded mRNA Library Prep Kit (Illumina,

663   cat# 20020594) and sequenced on a HiSeq2000.

664

665   For data analysis, reads were quality assessed using the FASTQC (v 0.11.8) and aligned to

666   the human reference genome (GRCh38_release_37) from GENCODE with Star aligner

667   (v2.7.3) using RSEM (v1.3.1) with default parameters. First, the human reference genome

668   was indexed using the GENCODE annotations (gencode.v37) with rsem-prepare-reference

669   from RSEM software. Next, rsem-calculate-expression was used to align the reads and

670   quantify the gene abundance. The output of rsem-calculate-expression gives separately the

671   read count and transcripts per million (TPM) value for each gene.

672

673   *Differential expression analysis*

674

675   Differential expression analysis was performed using gene read counts with DESeq2 package

676   (v 1.32.0) to produce LFC values and corresponding p-values (FDR) applying a Benjamini–

677   Hochberg correction for multiple testing. The heatmap was created using normalized gene

678   count values from Deseq2, using R gplots package heatmap.2 function with row scaling.

679

680   *Gene set enrichment analysis (GSEA)*

681

682   Gene set enrichment analysis was performed using the GSEA software downloaded from

683   http://www.gsea-msigdb.org/gsea/index.jsp (Mootha et al., 2003; Subramanian et al., 2005).

684   An expression dataset containing gene name and log2 (fold change) was generated based on

685   the RNA sequencing results and loaded to the software as the input file. The c5.all.v7.4 gene

686   matrix was used as the database of gene sets, and gene sets smaller than 10 or larger than

687   1000 in size were excluded for the analysis. The canonical HSC gene signature and specific

688   HSC gene signature were obtained from previous publication (Zhang et al., 2016), and the

689   liver cirrhosis signature was downloaded from Disgenet database (Piñero et al., 2020). Among

690   the 44 genes in the canonical HSC signature, 35 were found in our differential expression list.

691   Among the 122 genes in the specific HSC signature, 97 were found in our differential

692   expression list. Among the 103 genes in the liver cirrhosis signature, 69 were found in our

693   differential expression list. These genes were listed in Supplementary Table 8.

694

695   *Transwell migration assay*

696

697   HSCs were treated with DMSO or 1 µM NCMC for 48 hours or transfected with siRNAs for 72

698   hours in 6-well plates. HSCs were then trypsinized and counted to seed at 5,000-10,000 cells

699   per insert depending on donor and assay duration (Corning, cat# CLS3422) in serum-free

700   DMEM. Complete medium (with 10% FBS) was added to the bottom well to induce cell

701   migration through the pores (diameter: 8 µm) of the membrane at the bottom of the insert.

702   After the indicated assay time, cells were fixed with 4% paraformaldehyde at room

703   temperature for 15 min and stained with crystal violet (1% w/v in 20% methanol, Sigma, cat#

704   C0775) for 1 hour. Inserts were washed with DPBS, and the cells that had not migrated

705   through the pores and remained on the upper side of the membrane were removed with cotton

706   swabs. Images were taken using EVOS XL Core microscope with 10x lens under brightfield.

707

708   *Wound healing assay*

709

710   HSCs were plated in CytoSelect 24-well wound healing assay plates with inserts (Cell Biolabs,

711   cat# CBA-120) at 400,000 cells/well in complete medium. Eighteen hours after plating, inserts

712   were removed to generate a 0.9 mm wound field, and cells were incubated with complete

713   medium containing DMSO or NCMC for an additional 30 hours. Images were taken using

714   EVOS FL microscope.

715

716   *Proliferation assay*

717

718   HSCs were seeded in black-wall 96-well plates (Corning, cat# 3603) at 3,000 cells/well, and

719   18 hours later, DMSO and NCMC at different concentrations as indicated were added with six

720   replicates. One plate was fixed on each day with 4% paraformaldehyde for five days

721   consecutively and stored at 4°C until all plates were ready for staining with Hoechst.

722   ImageXpress Micro Confocal microscope (Molecular Devices) was used for taking four

723   images/well with 10x Plan Apo lens, and MetaXpress software was used for counting the

724   number of nuclei.

725

726   *Apoptosis analysis by flow cytometry*

727

728   HSCs were treated with DMSO or NCMC at indicated concentrations for 48 hours, followed

729   by trypsinization and staining with Annexin V and propidium iodide using Dead Cell Apoptosis

730   Kit (Invitrogen, cat# V13241) according to manufacturer's instructions. Cells were analyzed

731   using FACSAria II (BD Biosciences).

732

733   *Quiescence/cell cycle analysis by flow cytometry*

734

735   HSCs were treated with DMSO or NCMC at indicated concentrations for 48 hours, trypsinized,

736   harvested, washed with DPBS, and resuspended in 0.5mL DPBS. Cells were fixed by adding

737   4.5mL ice-cold 70% ethanol in a drop wise manner while vortexing and were then kept at -

738   20°C for at least 2 hours. Cells were washed twice with FACS buffer (DPBS supplemented

739   with 2% heated-inactivated filtered fetal bovine serum and 1mM EDTA) before resuspending

740   in FACS buffer at 1×10^6 cells/100μL. Cells were then incubated with Ki-67 antibody

741   (0.25µg/100µL, clone SolA15, Invitrogen, cat# 11-5698-82) in the dark for 30 min at room

742   temperature. After incubation, cells were washed twice with FACS buffer, followed by

743   incubation with propidium iodide staining solution (DPBS supplemented with 50µg/ml

744   propidium iodide (Invitrogen, cat# P3566), 10µg/ml RNase (Thermo Scientific, cat# EN0531)

745   and 2 mM $MgCl_2$) for another 20 min at room temperature before analysis by FACSAria II (BD

746   Biosciences).

747

748   *Calcium measurements*

749

750   Fluo-4 NW calcium assay starter kit (Invitrogen, F36206) was used to measure cytosolic

751   calcium according to the manufacturer's protocol in the presence and absence of 1 mM EGTA.

752   HSCs were plated on a Corning 96 well UV transparent plate 24 hours prior to analysis. Media

753   was removed and cells were washed with 1X calcium and magnesium chloride free PBS

754   before adding the dye mix with probenecid with and without EGTA to each well. Plates were

755   covered in aluminum foil and incubated at 37°C for 30 minutes. Plates were equilibrated to

756   room temperature for 30 mins prior to analysis. Measurements were performed on a Tecan

757   Infinite M Plex M-200 using I-control 2.0 software from Austria GmbH to measure fluorescence

758   intensity with excitation at 494 nm and emission at 516 nm. Readings were performed by

759   loading the plate immediately following treatment with DMSO or compounds at the indicated

760   concentration. All measurements were normalized to time 0 by subtracting the initial value for

761   each well. Based on this approach, the increase in Ca^{2+} levels measured for ionomycin may

762   be reduced due to a more rapid response to the compound. Measurements were plotted as

763   change in relative fluorescence unit (RFU) at 50% gain on the Y-axis relative to time 0 in

764   seconds on the X-axis using Graphpad Prism 8.4.3.

765

766   *Kinase array analysis*

767

768   HSCs from donor 3 were treated with DMSO or 1 µM NCMC for 1 hour or 18 hours. Cell

769   lysates were prepared and analyzed using the Proteome Profiler Human Phospho-Kinase

770   Array Kit (R&D Systems, cat# ARY003B) according to manufacturer's instructions. Scanned

771   films were quantified using ImageJ.

772

773   *RNAi-mediated depletion of gene expression*

774

775   HSCs were reverse transfected with siRNAs as indicated using Dharmafect-1 transfection

776   reagent (Horizon Discovery, cat# T-2001) according to manufacturer's instructions. For 12-

777   well plates, 60µL of 1µM siRNAs were added to 180µL Opti-MEM (Gibco, cat# 31985070) for

778   the final concentration of 50nM and then mixed with diluted Dharmafect-1 in Opti-MEM (1.2µL

779   Dharmafect-1 in 238.8µL Opti-MEM). After 30 min, HSCs resuspended in transfection medium

780   (DMEM supplemented with 16% FCS) were seeded in the wells containing the

781   siRNA/Dharmafect-1 mixture at 70,700 cells/mL in 720µL/well medium. Transfection in other

782   plate formats were scaled up or down accordingly based on surface area. Cells were

783   incubated with siRNAs and transfection reagents for 72 hours before analysis, unless

784   indicated otherwise.

785

786   The siRNAs used in this study are siGENOME SMARTpool siRNAs (Horizon Discovery) for

787   FYN (MQ-003140-04), HSP27 (M-005269-01), ERK1 (M-003592-03), ERK2 (M-003555-04),

788   FAK (M-003164-02), STAT5A (M-005169-02) and STAT5B (M-010539-02) and individual

789   siGENOME siRNAs for FYN (siRNA#1: D-003140-10, siRNA#2: D-003140-24).

790

791   *Cloning, lentivirus packaging and infection*

792

793   The cDNA encoding the dominant negative Y213A FYN mutant was amplified from the

794   plasmid pRK5 DN-Fyn (gift from Filippo Giancotti, Addgene plasmid # 16033) using the

795   following PCR primers: forward primer: 5'-CAT GCTAGC GCCACC

796 ATGGGCTGTGTGCAATGTAAGG-3'; reverse primer: 5'- AGC GAATTC

797 TTACAGGTTTTCACCAGGTTGGTAC-3'. The amplified PCR product was digested with NheI

798 and EcoRI enzymes and inserted into linearized pLJM1 plasmid (gift from David Sabatini,

799 Addgene, plasmid# 19319). Whole plasmid sequencing was performed to confirm that the DN-

800 FYN sequence was correct.

801

802 HEK 293 cells were transfected with pLJM1-eGFP or pLJM1-DN-FYN plasmid together with

803 lentivirus packing and envelope plasmids pMD2.G (gift from Didier Trono, Addgene plasmid#

804 12259) and psPAX2 (gift from Didier Trono, Addgene plasmid# 12260) using X-tremeGENE

805 9 DNA transfection reagent (Roche, cat# 6365779001) according to manufacturer's

806 instructions. For a 10cm dish of 293 cells, 30µL X-tremeGENE 9 reagent, 750ng psPAX2,

807 250ng pMD2.G and 1µg pLJM1-eGFP or pLJM1-DN-FYN were mixed in 500µL Opti-MEM and

808 incubated for 15 min before added to culture medium in a drop wise manner. 24 hours later,

809 culture medium was changed, and cells were incubated with fresh regular medium for another

810 24 hours. Conditioned medium containing virus was then collected and filtered through

811 0.45µm filters. HSCs were seeded to reach 30-40% confluency after 18 hours and then

812 infected with viruses. Polybrene (Sigma-Aldrich, cat# TR-1003-G) was used at a final

813 concentration of 10µg/mL to enhance infection efficiency.

814

815 *Western blot*

816

817 Cells were pelleted and lysed with RIPA buffer (150 mM sodium chloride, 1.0% Triton X-100,

818 0.5% sodium deoxycholate, 0.1% SDS (sodium dodecyl sulfate) and 50 mM Tris, pH 8.0)

819 supplemented with protease inhibitors (Thermo Scientific, cat# 87786) and phosphatase

820 inhibitors (Thermo Scientific, cat# 78420). Cell lysates were centrifuged to remove debris.

821 Protein concentrations were measured using Pierce™ BCA Protein Assay Kit (Thermo

822 Scientific, cat# 23227). Bolt™ LDS Sample Buffer (Invitrogen, cat# B0007) and Bolt™ Sample

823 Reducing Agent (Invitrogen, cat# B0009) were added to cell lysates and the sample mixture

31

824 was boiled for 10 min before loading. Bolt™ 4 to 12% Bis-Tris gels (Invitrogen, cat#

825 NW04120BOX) were used for electrophoresis, followed by transferring with iBlot 2 Dry Blotting

826 System (Invitrogen, cat# IB21002S). Membranes were blocked with 1% BSA (Thermo

827 Scientific, cat# 37520, for phospho-Src family) or 3% milk (Lab Scientific, cat# M0841, for

828 other proteins) at room temperature for 1 hour and incubated with primary antibody at 4°C for

829 two days (for FYN) or overnight (for other proteins). Membranes were washed three times with

830 Tris Buffered Saline-Tween (TBST) buffer (Boston BioProducts, cat# IBB-181-6), incubated

831 with secondary antibody for another 1 hour, washed three times with TBST buffer, and then

832 incubated with SuperSignal™ West Pico PLUS chemiluminescent substrates (Thermo

833 Scientific, cat# 34580) for 5 min before exposure to film (Ece Scientific Co, cat# E3018). The

834 following antibodies were used: FYN antibody (1:1000, Cell Signaling Technology, cat# 4023),

835 phospho-Src family antibody (1:1000, Cell Signaling Technology, cat# 6943), HRP-β-Actin

836 antibody (Santa Cruz Biotechnology, cat# sc-47778), phospho-p44/42 MAPK (Erk1/2)

837 (Thr202/Tyr204) antibody (1:1000, Cell Signaling Technology, cat# 4370), and goat anti-rabbit

838 IgG secondary antibody (Invitrogen, cat# 32460).

839

840 *Data availability*

841

842 RNA sequencing data produced in this study have been submitted to GEO (GSE180980). The

843 full dataset will be accessible when released.

844

845 **Acknowledgements**

852 Sequencing Core, MGH Center for Regenerative Medicine Flow Cytometry Facility, and MGH

853 Program in Membrane Biology Microscopy Core for their support. This work was funded

854 through a grant from Boehringer Ingelheim.

855

856 **Competing interests**

857 MB, JFR, and JFD are employees of Boehringer Ingelheim. ACM receives funding from

858 Bristol-Myers Squibb and GlaxoSmithKline for unrelated projects and is a consultant for Circ

859 Bio.

860

861 **References**

862

863 Alsamman, S., Christenson, S. A., Yu, A., Ayad, N. M. E., Mooring, M. S., Segal, J. M., . . .
864   Chen, J. Y. (2020). Targeting acid ceramidase inhibits YAP/TAZ signaling to reduce
865   fibrosis in mice. *Sci Transl Med*, *12*(557).
866   https://doi.org/10.1126/scitranslmed.aay8798
867 Anstee, Q. M., Reeves, H. L., Kotsiliti, E., Govaere, O., & Heikenwalder, M. (2019). From
868   NASH to HCC: current concepts and future challenges. *Nat Rev Gastroenterol Hepatol*,
869   *16*(7), 411-428. https://doi.org/10.1038/s41575-019-0145-7
870 Baell, J. B., & Nissink, J. W. M. (2018). Seven Year Itch: Pan-Assay Interference Compounds
871   (PAINS) in 2017-Utility and Limitations. *ACS Chem Biol*, *13*(1), 36-44.
872   https://doi.org/10.1021/acschembio.7b00903
873 Bataller, R., & Brenner, D. A. (2005). Liver fibrosis. *J Clin Invest*, *115*(2), 209-218.
874   https://doi.org/10.1172/JCI24282
875 Benyon, R. C., & Iredale, J. P. (2000). Is liver fibrosis reversible? *Gut*, *46*(4), 443-446.
876   https://doi.org/10.1136/gut.46.4.443
877 Bonis, P. A., Friedman, S. L., & Kaplan, M. M. (2001). Is liver fibrosis reversible? *N Engl J*
878   *Med*, *344*(6), 452-454. https://doi.org/10.1056/NEJM200102083440610
879 Bosch, M., Gil, J., Bachs, O., & Agell, N. (1998). Calmodulin inhibitor W13 induces sustained
880   activation of ERK2 and expression of p21(cip1). *J Biol Chem*, *273*(34), 22145-22150.
881   https://doi.org/10.1074/jbc.273.34.22145
882 Chen, C. Z., Peng, Y. X., Wang, Z. B., Fish, P. V., Kaar, J. L., Koepsel, R. R., . . . Raghunath,
883   M. (2009). The Scar-in-a-Jar: studying potential antifibrotic compounds from the
884   epigenetic to extracellular level in a single well. *Br J Pharmacol*, *158*(5), 1196-1209.
885   https://doi.org/10.1111/j.1476-5381.2009.00387.x
886 Chen, J. Y., Newcomb, B., Zhou, C., Pondick, J. V., Ghoshal, S., York, S. R., . . . Mullen, A.
887   C. (2017). Tricyclic Antidepressants Promote Ceramide Accumulation to Regulate
888   Collagen Production in Human Hepatic Stellate Cells. *Sci Rep*, *7*, 44867.
889   https://doi.org/10.1038/srep44867
890 Chuderland, D., Marmor, G., Shainskaya, A., & Seger, R. (2020). Calcium-Mediated
891   Interactions Regulate the Subcellular Localization of Extracellular Signal-Regulated
892   Kinases (ERKs). *Cell Physiol Biochem*, *54*(3), 474-492.
893   https://doi.org/10.33594/000000231
894 Cook, S. J., Beltman, J., Cadwallader, K. A., McMahon, M., & McCormick, F. (1997).
895   Regulation of mitogen-activated protein kinase phosphatase-1 expression by

896   extracellular signal-related kinase-dependent and Ca2+-dependent signal pathways in
897   Rat-1 cells. *J Biol Chem*, *272*(20), 13309-13319.
898   https://doi.org/10.1074/jbc.272.20.13309
899   Dittmar, M., Lee, J. S., Whig, K., Segrist, E., Li, M., Jurado, K., . . . Cherry, S. (2020). Drug
900   repurposing screens reveal FDA approved drugs active against SARS-Cov-2. *bioRxiv*,
901   2020.2006.2019.161042. https://doi.org/10.1101/2020.06.19.161042
902   Du, G., Wang, J., Zhang, T., Ding, Q., Jia, X., Zhao, X., . . . Lu, Y. (2020). Targeting Src family
903   kinase member Fyn by Saracatinib attenuated liver fibrosis in vitro and in vivo. *Cell*
904   *Death Dis*, *11*(2), 118. https://doi.org/10.1038/s41419-020-2229-2
905   Eisenberg, E., & Levanon, E. Y. (2013). Human housekeeping genes, revisited. *Trends Genet*,
906   *29*(10), 569-574. https://doi.org/10.1016/j.tig.2013.05.010
907   Falize, L., Guillygomarc'h, A., Perrin, M., Lainé, F., Guyader, D., Brissot, P., . . . Deugnier, Y.
908   (2006). Reversibility of hepatic fibrosis in treated genetic hemochromatosis: a study of
909   36 cases. *Hepatology*, *44*(2), 472-477. https://doi.org/10.1002/hep.21260
910   Filvaroff, E., Stern, D. F., & Dotto, G. P. (1990). Tyrosine phosphorylation is an early and
911   specific event involved in primary keratinocyte differentiation. *Mol Cell Biol*, *10*(3),
912   1164-1173. https://doi.org/10.1128/mcb.10.3.1164-1173.1990
913   Friedman, S. L. (2008). Hepatic stellate cells: protean, multifunctional, and enigmatic cells of
914   the liver. *Physiol Rev*, *88*(1), 125-172. https://doi.org/10.1152/physrev.00013.2007
915   Friedman, S. L., Roll, F. J., Boyles, J., & Bissell, D. M. (1985). Hepatic lipocytes: the principal
916   collagen-producing cells of normal rat liver. *Proc Natl Acad Sci U S A*, *82*(24), 8681-
917   8685. https://doi.org/10.1073/pnas.82.24.8681
918   Geerts, A. (2001). History, heterogeneity, developmental biology, and functions of quiescent
919   hepatic stellate cells. *Semin Liver Dis*, *21*(3), 311-335. https://doi.org/10.1055/s-2001-
920   17550
921   Good, R. B., Eley, J. D., Gower, E., Butt, G., Blanchard, A. D., Fisher, A. J., & Nanthakumar,
922   C. B. (2019). A high content, phenotypic 'scar-in-a-jar' assay for rapid quantification of
923   collagen fibrillogenesis using disease-derived pulmonary fibroblasts. *BMC Biomedical*
924   *Engineering*, *1*(1), 14. https://doi.org/10.1186/s42490-019-0014-z
925   Guo, Y. C., & Lu, L. G. (2020). Antihepatic Fibrosis Drugs in Clinical Trials. *J Clin Transl*
926   *Hepatol*, *8*(3), 304-312. https://doi.org/10.14218/JCTH.2020.00023
927   Hernandez-Gea, V., & Friedman, S. L. (2011). Pathogenesis of liver fibrosis. *Annu Rev Pathol*,
928   *6*, 425-456. https://doi.org/10.1146/annurev-pathol-011110-130246
929   Huang, M., Liu, B., Liu, R., Li, J., Chen, J., Jiang, F., . . . Liu, T. (2018). Aglycone Polyether
930   Nanchangmycin and Its Homologues Exhibit Apoptotic and Antiproliferative Activities
931   against Cancer Stem Cells. *ACS Pharmacol Transl Sci*, *1*(2), 84-95.
932   https://doi.org/10.1021/acsptsci.8b00007
933   Huczyński, A. (2012). Polyether ionophores-promising bioactive molecules for cancer therapy.
934   *Bioorg Med Chem Lett*, *22*(23), 7002-7010. https://doi.org/10.1016/j.bmcl.2012.09.046
935   Jones, K. T., & Sharpe, G. R. (1994). Thapsigargin raises intracellular free calcium levels in
936   human keratinocytes and inhibits the coordinated expression of differentiation markers.
937   *Exp Cell Res*, *210*(1), 71-76. https://doi.org/10.1006/excr.1994.1011
938   Karlsen, T. H., Folseraas, T., Thorburn, D., & Vesterhus, M. (2017). Primary sclerosing
939   cholangitis - a comprehensive review. *J Hepatol*, *67*(6), 1298-1323.
940   https://doi.org/10.1016/j.jhep.2017.07.022
941   Kaspar, J. W., & Jaiswal, A. K. (2011). Tyrosine phosphorylation controls nuclear export of
942   Fyn, allowing Nrf2 activation of cytoprotective gene expression. *FASEB J*, *25*(3), 1076-
943   1087. https://doi.org/10.1096/fj.10-171553
944   Kevin Ii, D. A., Meujo, D. A., & Hamann, M. T. (2009). Polyether ionophores: broad-spectrum
945   and promising biologically active molecules for the control of drug-resistant bacteria
946   and parasites. *Expert Opin Drug Discov*, *4*(2), 109-146.
947   https://doi.org/10.1517/17460440802661443
948   Kisseleva, T., Cong, M., Paik, Y., Scholten, D., Jiang, C., Benner, C., . . . Brenner, D. A. (2012).
949   Myofibroblasts revert to an inactive phenotype during regression of liver fibrosis. *Proc*
950   *Natl Acad Sci U S A*, *109*(24), 9448-9453. https://doi.org/10.1073/pnas.1201840109

951   Leite, S. B., Roosens, T., El Taghdouini, A., Mannaerts, I., Smout, A. J., Najimi, M., . . . van
952   Grunsven, L. A. (2016). Novel human hepatic organoid model enables testing of drug-
953   induced liver fibrosis in vitro. *Biomaterials*, *78*, 1-10.
954   https://doi.org/10.1016/j.biomaterials.2015.11.026
955   Li, J.-Q., Huang, M., Zhang, Y.-N., Liu, R., Zhang, Z.-R., Zhang, Q.-Y., . . . Liu, T. (2020).
956   Aglycone polyether ionophores as broad-spectrum agents inhibit multiple enveloped
957   viruses including SARS-CoV-2 in vitro and successfully cure JEV infected mice.
958   *bioRxiv*, 2020.2010.2027.354563. https://doi.org/10.1101/2020.10.27.354563
959   Maher, J. J., & McGuire, R. F. (1990). Extracellular matrix gene expression increases
960   preferentially in rat lipocytes and sinusoidal endothelial cells during hepatic fibrosis in
961   vivo. *J Clin Invest*, *86*(5), 1641-1648. https://doi.org/10.1172/JCI114886
962   Matlock, M. K., Hughes, T. B., Dahlin, J. L., & Swamidass, S. J. (2018). Modeling Small-
963   Molecule Reactivity Identifies Promiscuous Bioactive Compounds. *J Chem Inf Model*,
964   *58*(8), 1483-1500. https://doi.org/10.1021/acs.jcim.8b00104
965   Maurer, B., Kollmann, S., Pickem, J., Hoelbl-Kovacic, A., & Sexl, V. (2019). STAT5A and
966   STAT5B-Twins with Different Personalities in Hematopoiesis and Leukemia. *Cancers
967   (Basel)*, *11*(11). https://doi.org/10.3390/cancers11111726
968   Mederacke, I., Hsu, C. C., Troeger, J. S., Huebener, P., Mu, X., Dapito, D. H., . . . Schwabe,
969   R. F. (2013). Fate tracing reveals hepatic stellate cells as dominant contributors to liver
970   fibrosis independent of its aetiology. *Nat Commun*, *4*, 2823.
971   https://doi.org/10.1038/ncomms3823
972   Mootha, V. K., Lindgren, C. M., Eriksson, K. F., Subramanian, A., Sihag, S., Lehar, J., . . .
973   Groop, L. C. (2003). PGC-1alpha-responsive genes involved in oxidative
974   phosphorylation are coordinately downregulated in human diabetes. *Nat Genet*, *34*(3),
975   267-273. https://doi.org/10.1038/ng1180
976   Morgan, A. J., & Jacob, R. (1994). Ionomycin enhances Ca2+ influx by stimulating store-
977   regulated cation entry and not by a direct action at the plasma membrane. *Biochem J*,
978   *300 (Pt 3)*, 665-672. https://doi.org/10.1042/bj3000665
979   Murphy, S. L., Xu, J., Kochanek, K. D., Arias, E., & Tejada-Vera, B. (2021). Deaths: Final Data
980   for 2018. *Natl Vital Stat Rep*, *69*(13), 1-83.
981   Pagès, G., Lenormand, P., L'Allemain, G., Chambard, J. C., Meloche, S., & Pouysségur, J.
982   (1993). Mitogen-activated protein kinases p42mapk and p44mapk are required for
983   fibroblast proliferation. *Proc Natl Acad Sci U S A*, *90*(18), 8319-8323.
984   https://doi.org/10.1073/pnas.90.18.8319
985   Pang, M., & Zhuang, S. (2010). Histone deacetylase: a potential therapeutic target for fibrotic
986   disorders. *J Pharmacol Exp Ther*, *335*(2), 266-272.
987   https://doi.org/10.1124/jpet.110.168385
988   Piñero, J., Ramírez-Anguita, J. M., Saüch-Pitarch, J., Ronzano, F., Centeno, E., Sanz, F., &
989   Furlong, L. I. (2020). The DisGeNET knowledge platform for disease genomics: 2019
990   update. *Nucleic Acids Res*, *48*(D1), D845-D855. https://doi.org/10.1093/nar/gkz1021
991   Rausch, K., Hackett, B. A., Weinbren, N. L., Reeder, S. M., Sadovsky, Y., Hunter, C. A., . . .
992   Cherry, S. (2017). Screening Bioactives Reveals Nanchangmycin as a Broad
993   Spectrum Antiviral Active against Zika Virus. *Cell Rep*, *18*(3), 804-815.
994   https://doi.org/10.1016/j.celrep.2016.12.068
995   Ribeiro, D., Freitas, M., Rocha, S., Lima, J. L. F. C., Carvalho, F., & Fernandes, E. (2018).
996   Calcium Pathways in Human Neutrophils-The Extended Effects of Thapsigargin and
997   ML-9. *Cells*, *7*(11). https://doi.org/10.3390/cells7110204
998   Rusanescu, G., Qi, H., Thomas, S. M., Brugge, J. S., & Halegoua, S. (1995). Calcium influx
999   induces neurite growth through a Src-Ras signaling cassette. *Neuron*, *15*(6), 1415-
1000   1425. https://doi.org/10.1016/0896-6273(95)90019-5
1001 Sodhi, K., Srikanthan, K., Goguet-Rubio, P., Nichols, A., Mallick, A., Nawab, A., . . . Shapiro,
1002   J. I. (2017). pNaKtide Attenuates Steatohepatitis and Atherosclerosis by Blocking
1003   Na/K-ATPase/ROS Amplification in C57Bl6 and ApoE Knockout Mice Fed a Western
1004   Diet. *Sci Rep*, *7*(1), 193. https://doi.org/10.1038/s41598-017-00306-5

Subramanian, A., Tamayo, P., Mootha, V. K., Mukherjee, S., Ebert, B. L., Gillette, M. A., . . . Mesirov, J. P. (2005). Gene set enrichment analysis: a knowledge-based approach for interpreting genome-wide expression profiles. *Proc Natl Acad Sci U S A, 102*(43), 15545-15550. https://doi.org/10.1073/pnas.0506580102

Sun, Y., Zhou, X., Liu, J., Bao, K., Zhang, G., Tu, G., . . . Deng, Z. (2002). 'Streptomyces nanchangensis', a producer of the insecticidal polyether antibiotic nanchangmycin and the antiparasitic macrolide meilingmycin, contains multiple polyketide gene clusters. *Microbiology (Reading), 148*(Pt 2), 361-371. https://doi.org/10.1099/00221287-148-2-361

Sun, Y. M., Chen, S. Y., & You, H. (2020). Regression of liver fibrosis: evidence and challenges. *Chin Med J (Engl), 133*(14), 1696-1702. https://doi.org/10.1097/CM9.0000000000000835

Svenningsen, E. B., Thyrsted, J., Blay-Cadanet, J., Liu, H., Lin, S., Villameriel, J. M., . . . Poulsen, T. B. (2020). Ionophore antibiotic X-206 is a potent and selective inhibitor of SARS-CoV-2 infection in vitro. *bioRxiv*, 2020.2006.2014.149153. https://doi.org/10.1101/2020.06.14.149153

Tian, J., & Xie, Z. J. (2008). The Na-K-ATPase and calcium-signaling microdomains. *Physiology (Bethesda), 23*, 205-211. https://doi.org/10.1152/physiol.00008.2008

Troeger, J. S., Mederacke, I., Gwak, G. Y., Dapito, D. H., Mu, X., Hsu, C. C., . . . Schwabe, R. F. (2012). Deactivation of hepatic stellate cells during liver fibrosis resolution in mice. *Gastroenterology, 143*(4), 1073-1083.e1022. https://doi.org/10.1053/j.gastro.2012.06.036

Xia, Z., Dudek, H., Miranti, C. K., & Greenberg, M. E. (1996). Calcium influx via the NMDA receptor induces immediate early gene transcription by a MAP kinase/ERK-dependent mechanism. *J Neurosci, 16*(17), 5425-5436.

Xu, Y., Sun, T., Zeng, K., Xu, M., Chen, J., Xu, X., . . . Mao, X. (2020). Anti-bacterial and anti-viral nanchangmycin displays anti-myeloma activity by targeting Otub1 and c-Maf. *Cell Death Dis, 11*(9), 818. https://doi.org/10.1038/s41419-020-03017-4

Yoon, S., Kang, G., & Eom, G. H. (2019). HDAC Inhibitors: Therapeutic Potential in Fibrosis-Associated Human Diseases. *Int J Mol Sci, 20*(6). https://doi.org/10.3390/ijms20061329

Younossi, Z. M., Koenig, A. B., Abdelatif, D., Fazel, Y., Henry, L., & Wymer, M. (2016). Global epidemiology of nonalcoholic fatty liver disease-Meta-analytic assessment of prevalence, incidence, and outcomes. *Hepatology, 64*(1), 73-84. https://doi.org/10.1002/hep.28431

Zhang, D. Y., Goossens, N., Guo, J., Tsai, M. C., Chou, H. I., Altunkaynak, C., . . . Friedman, S. L. (2016). A hepatic stellate cell gene expression signature associated with outcomes in hepatitis C cirrhosis and hepatocellular carcinoma after curative resection. *Gut, 65*(10), 1754-1764. https://doi.org/10.1136/gutjnl-2015-309655

Zhao, X. K., Cheng, Y., Liang Cheng, M., Yu, L., Mu, M., Li, H., . . . Zhang, Q. (2016). Focal Adhesion Kinase Regulates Fibroblast Migration via Integrin beta-1 and Plays a Central Role in Fibrosis. *Sci Rep, 6*, 19276. https://doi.org/10.1038/srep19276

Zhao, X. K., Yu, L., Cheng, M. L., Che, P., Lu, Y. Y., Zhang, Q., . . . Ding, Q. (2017). Focal Adhesion Kinase Regulates Hepatic Stellate Cell Activation and Liver Fibrosis. *Sci Rep, 7*(1), 4032. https://doi.org/10.1038/s41598-017-04317-0

Zhou, J., Yi, Q., & Tang, L. (2019). The roles of nuclear focal adhesion kinase (FAK) on Cancer: a focused review. *J Exp Clin Cancer Res, 38*(1), 250. https://doi.org/10.1186/s13046-019-1265-1
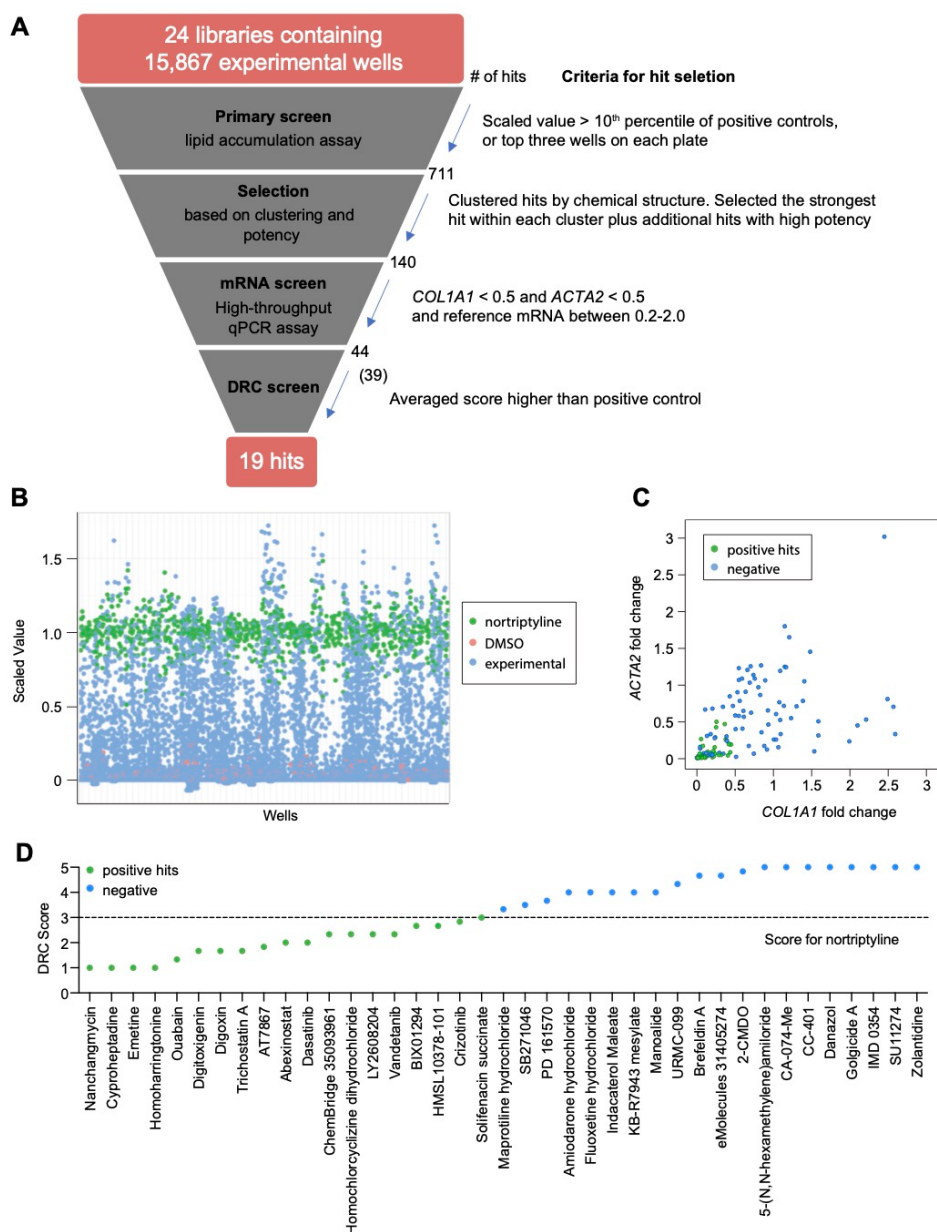
**Figure 1. High-throughput small molecule screen in primary human HSCs**
A. Overview of the small molecule screen. The number of candidate compounds (# of hits) is indicated at each step. The number in parenthesis represents the number of compounds tested in the final dose response curve (DRC) analysis due to availability. **B.** Results of the primary lipid accumulation screen. Each dot indicates the mean scaled value of two replicates for each condition at 48 hours. Red dots represent negative control wells (DMSO), green dots represent positive control wells (nortriptyline, 27 μM), and blue dots represent experimental wells. **C.** Results of the secondary mRNA screen. Each dot indicates the mean fold change of *ACTA2* and *COL1A1* after treatment with compounds (normalized to DMSO controls). *PSMB2* was used as the reference gene (n=4). Green dots represent positive hits (<0.5), and blue dots represent non-hits (negative). **D.** Dose-response curves were plotted for 39 compounds and were scored by three researchers independently. The mean score for each compound was plotted. The dotted line indicates the score of the positive control nortriptyline. Green dots represent positive hits, and blue dots represent non-hits (negative). This figure has two supplements.
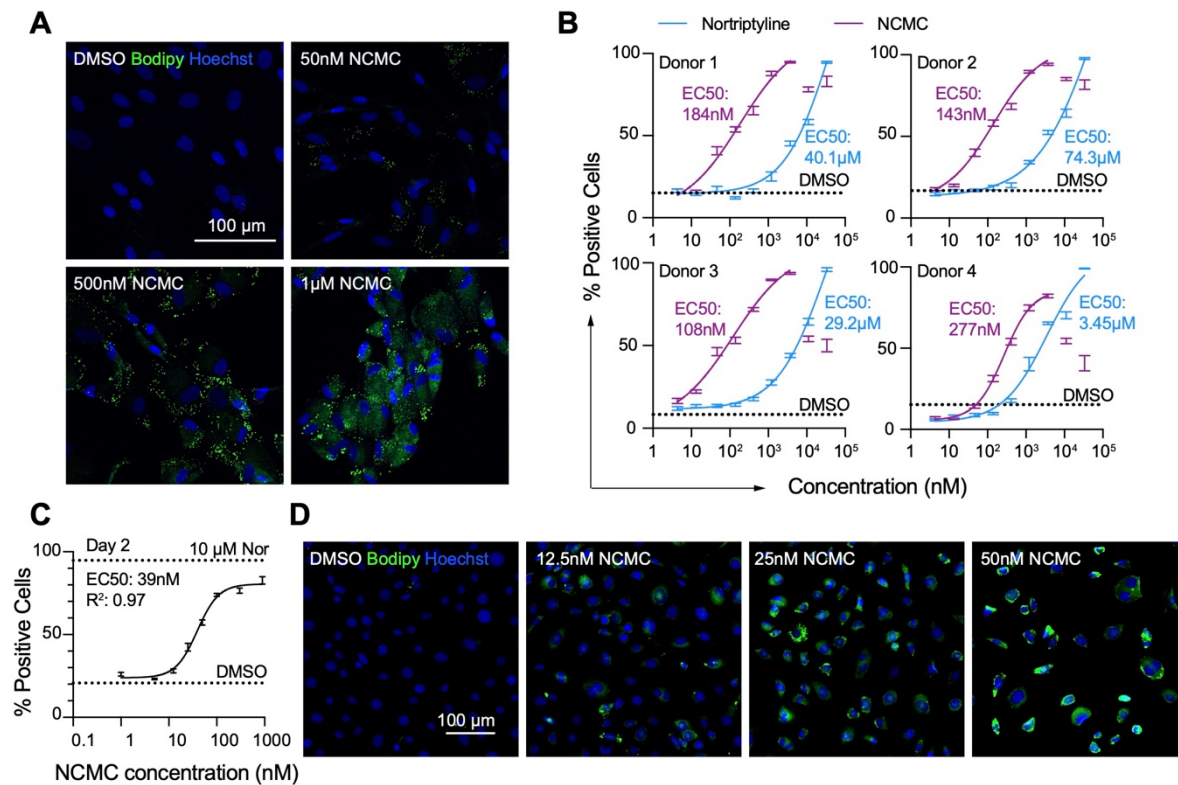
Figure 2. NCMC induces lipid accumulation in HSCs

A. Representative microscopic images of HSCs treated with DMSO and NCMC for 48 hours. Cells were stained with Bodipy to identify lipid droplets (green) and Hoechst to define nuclei (blue). Scale bar represents 100 μm. **B.** Dose response curves for NCMC (purple) and nortriptyline (blue) in HSCs isolated from four different human donors at 48 hours. Dotted line represents the mean percentage of Bodipy-positive cells in DMSO control wells. Error bars represent mean ± SEM (n=12). One experiment was performed for each of four donor lines. Curves were generated by fitting the data to a sigmoidal model. The data from the highest two concentrations of NCMC treatment (11 and 33 μM) were not used for fitting due to higher toxicity at these concentrations, as indicated by cell number (Figure 2 – figure supplement 1). **C.** Dose response curve for NCMC treatment in murine primary HSCs at 48 hours. Dotted lines represent the averaged percentage of Bodipy-positive cells in DMSO negative control wells (lower) and nortriptyline positive control wells (10 μM, upper). Error bars represent mean ± SEM (n=6). **D.** Representative images of murine HSCs treated with DMSO and NCMC for 48 hours and stained with Bodipy to identify lipid droplets (green) and Hoechst to define nuclei (blue). Scale bar represents 100 μm. This figure has two supplements.

1089
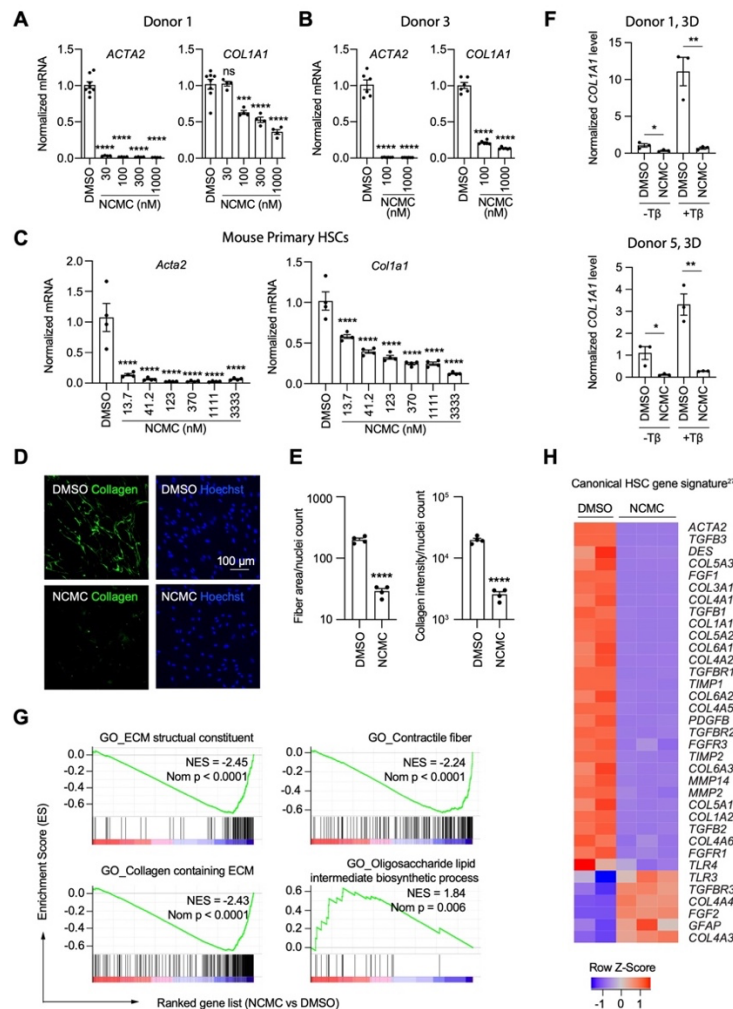
Figure 3. NCMC inhibits expression of fibrotic genes in HSCs
A-B. Effect of 48 hr NCMC treatment on *ACTA2* and *COL1A1* in HSCs from human donors 1 (**A**) and 3 (**B**). Error bars represent mean ± SEM (n=3). Data are representative of three independent experiments. ns indicates not significant, *** indicates $p < 0.001$, and **** indicates $p < 0.0001$ (one-way ANOVA test). **C.** Effect of 48-hour NCMC treatment on *Acta2* and *Col1a1* in primary mouse HSCs. Error bars represent mean ± SEM (n=4). Data are representative of three independent experiments. **** indicates $p < 0.0001$ (one-way ANOVA test). **D-E.** Effect of 48hr NCMC treatment (1 µM) on collagen deposition in ECM. **D**: representative images. Scale bar represents 100 µm. Collagen protein is indicated in green and nuclei for the same field are indicated in blue. **E**: quantified results. Error bars represent mean ± SEM (n=4). Data are representative of three independent experiments. **** indicates $p < 0.0001$ (Student's t-test). **F.** qPCR analysis of *COL1A1* in HSC-hepatocyte spheroids treated with NCMC with and without TGF-β (Tβ). Error bars represent mean ± SEM (n=3). One experiment was performed for each donor shown. * indicates $p < 0.05$ (Student's t-test) and ** indicates $p < 0.01$ (Student's t-test). Analysis was performed on day 3 (3D). **G-H.** RNA sequencing analysis of HSCs (donor 1) treated with DMSO or 1 µM NCMC for 48 hours. **G:** Representative gene sets from the gene set enrichment analysis (GSEA). NES refers to normalized enrichment score. Nom P refers to Nominal P value. Vertical black lines refer to affected genes in the indicated signatures. Red color indicates positive correlation, and blue color indicates negative correlation. **H**: Heatmap showing RNA-seq expression for the canonical HSC gene signature (Zhang et al., 2016). All genes from the signature that are expressed in HSCs (with a minimum of five reads) were shown regardless of their expression patterns. Z-score values are also provided in Supplementary Table 8. This figure has one supplement.
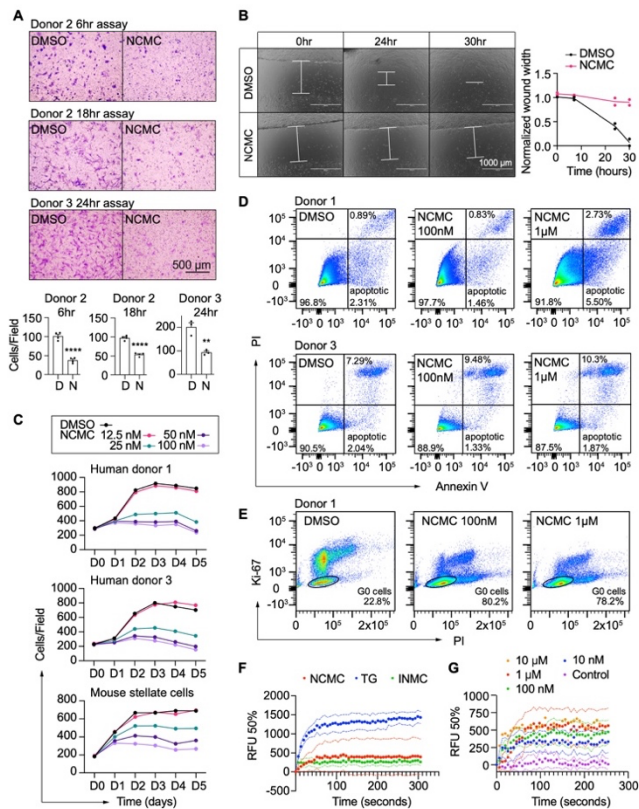
Figure 4. NCMC inhibits HSC migration and proliferation and increases cytosolic calcium concentration

A. Transwell migration assay results of HSCs treated with DMSO or 1 µM NCMC for 48hr. Top: representative images. Scale bar represents 500 µm. Bottom: quantification of migrated cells (n=3 for each experiment). ** indicates p < 0.01, and **** indicates p < 0.0001 (Student's t-test). **B.** Wound healing assay results of HSCs treated with DMSO or NCMC. HSCs were seeded in complete medium, and immediately after generating the wound field, DMSO and 1 µM NCMC were added. The closure of the wound field was monitored for up to 30 hours as indicated. Left: representative images. White bars highlight the width of the wound field. Scale bar represents 1000 µm. Right: quantification of wound width. (n=2). Data are representative of three independent experiments. **C.** Cell count for HSCs treated with DMSO or NCMC over the indicated time in days. Top: human HSCs from donor 1. Middle: human HSCs from donor 3. Bottom: mouse HSCs. Error bars represent mean ± SEM (n=6) but are too small to be visualized. One experiment was performed for each HSC line shown. **D.** Flow cytometry analysis of Annexin V and propidium iodide (PI) stained HSCs from human donor 1 (top) and 3 (bottom) treated with DMSO or NCMC for 48 hours. Plots are representative of two independent experiments. **E.** Flow cytometry analysis of Ki-67 and PI stained HSCs from human donor 1 treated with DMSO or NCMC for 24 hours. Plots are representative of two independent experiments. **F.** Measurement of cytosolic calcium level using fluo-4 NW. HSCs from donor 3 were pre-loaded with fluo-4 NW and fluorescent intensity was read immediately after adding compounds (NCMC: nanchangmycin (red), TG: thapsigargin (blue), INMC: ionomycin (green)). The plot demonstrates results from three independent experiments. Solid dots represent mean, and dotted lines represent SEM (n=3). RFU: Relative fluorescence unit. **G.** Measurement of cytosolic calcium level after adding NCMC at indicated concentrations in HSCs from donor 3 (magenta: control (no compound, no DMSO), blue: 10 nM, green: 100 nM, red 1 µM, orange: 10 µM). The plot demonstrates results from one experiment for 10 µM and five independent experiments for the other concentrations. Solid dots represent mean, and dotted lines represent SEM (n=3). This figure has two supplements.

40
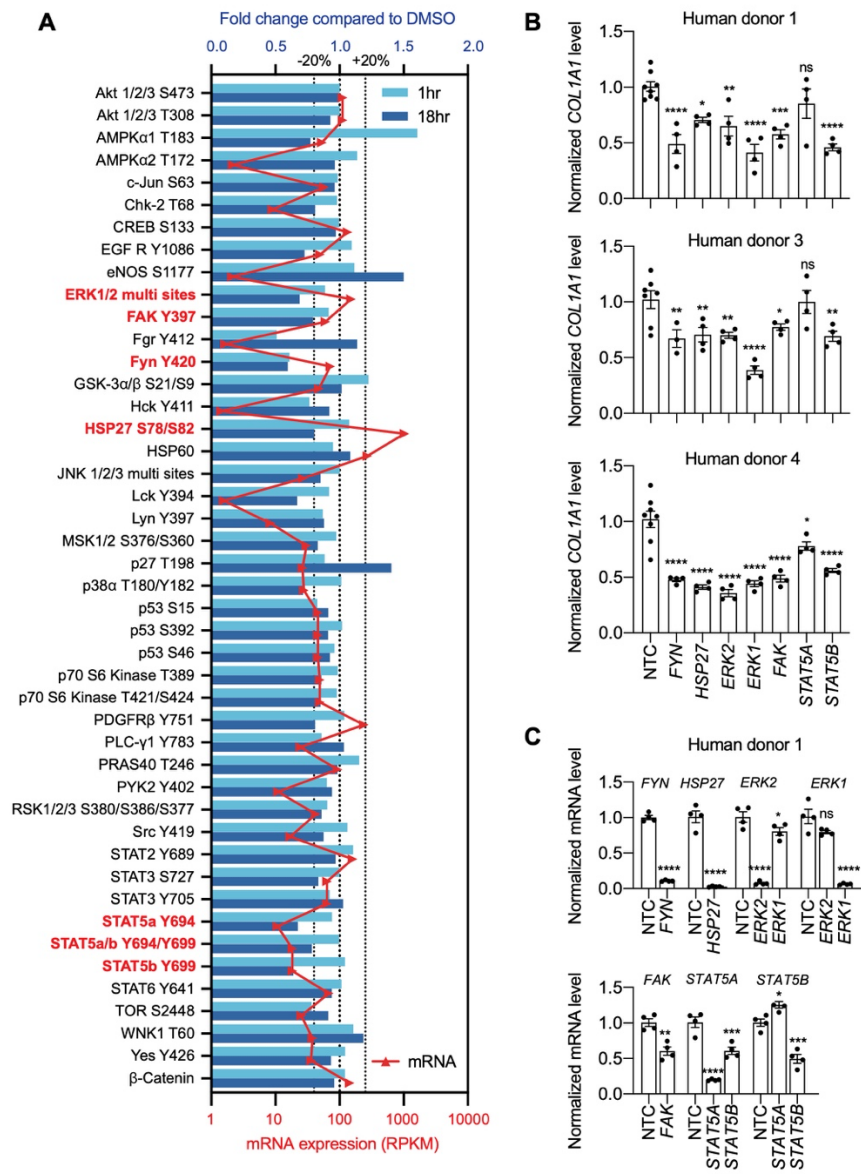
1144

Figure 5. Multiple kinases mediate the effect of NCMC on *COL1A1* expression
A. Kinase array analysis of HSCs treated with DMSO or 1 µM NCMC for 1 or 18 hours. Blue bars indicate mean fold change (n=2) in phosphorylation at specified sites in NCMC-treated cells compared to DMSO-treated cells at 1 hour (light blue) or 18 hours (dark blue). Red triangles indicate the mean RPKM of each corresponding kinase mRNA based on RNA sequencing of HSCs (Chen et al., 2017). The three dotted lines represent 20% increase/decrease or no change in phosphorylation. Kinases highlighted in red were chosen for further investigation. **B.** The expression of each candidate kinase gene was depleted using pooled siRNAs, and after 72 hours, *COL1A1* level was determined by qRT-PCR in HSCs isolated from human donor 1 (top), 3 (middle), or 4 (bottom). A non-targeting siRNA is used as a control (NTC). Error bars represent mean ± SEM (n ≥ 4, as indicated by the number of dots). ns indicates not significant (p > 0.05), * indicates p < 0.05, ** indicates p < 0.01, *** indicates p < 0.001, and **** indicates p < 0.0001 (one-way ANOVA test). **C.** Knockdown efficiency of each siRNA pool in HSCs from human donor 1. Error bars represent mean ± SEM (n ≥ 4). ns indicates not significant (p > 0.05), * indicates p < 0.05, ** indicates p < 0.01, *** indicates p < 0.001, and **** indicates p < 0.0001 (Student's t-test performed for *FYN*, *HSP27*, and *FAK* depletion, and one-way ANOVA test performed for *ERK1*, *ERK2*, *STAT5A* and *STAT5B* depletion). This figure has one supplement.

1163
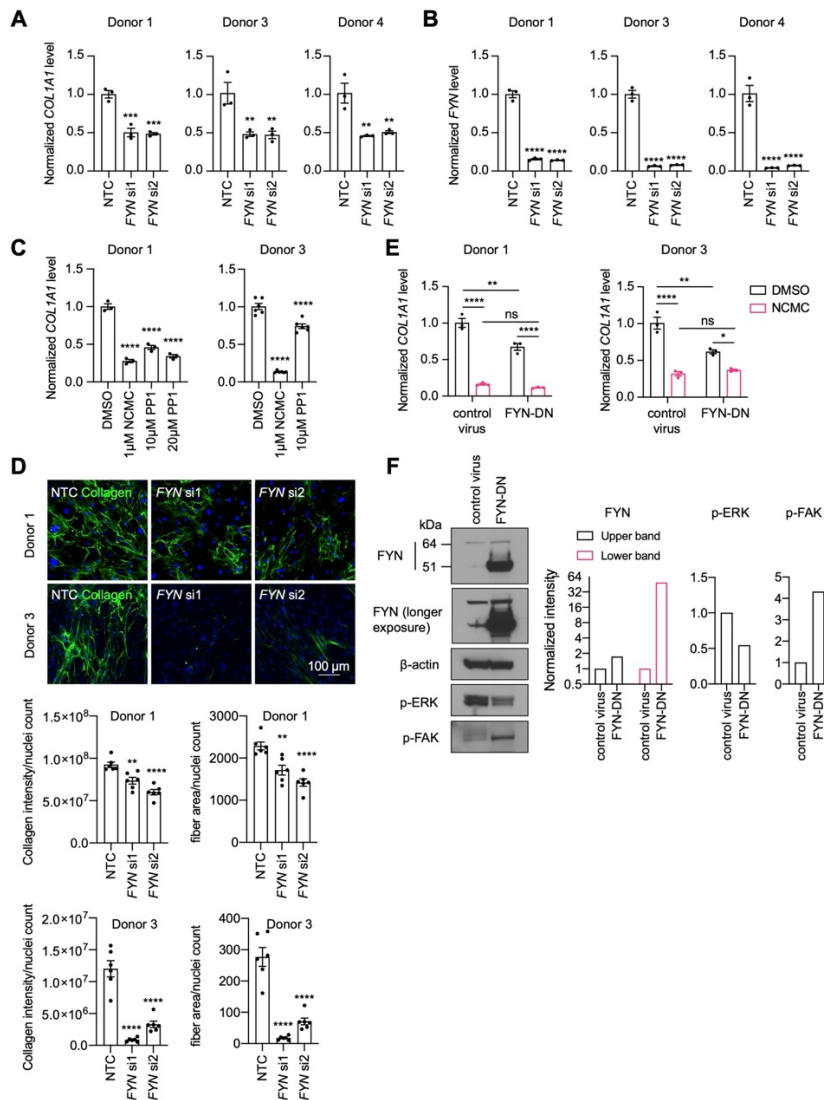
Figure 6. FYN/ERK pathway regulates collagen expression

A-B. *FYN* was depleted in HSCs with two siRNAs (si1 and si2). The expression levels of *COL1A1* (**A**) and *FYN* (**B**) were analyzed by qPCR after 72 hours in comparison to a non-targeting control siRNA (NTC). Error bars represent mean ± SEM (n=3) for each of three donor lines. ** indicates $p < 0.01$, *** indicates $p < 0.001$, and **** indicates $p < 0.0001$ (one-way ANOVA test). **C.** HSCs were treated with NCMC or 1-Naphthyl PP1 (PP1) for 48 hours. *COL1A1* level was analyzed by qPCR. Error bars represent mean ± SEM (n=3 for donor 1, and n=6 for donor 3). Data are representative of three independent experiments for donor 1 and experiment for donor 3. **** indicates $p < 0.0001$ (one-way ANOVA test). **D.** Effect of FYN-depletion on collagen deposition in ECM. Top: representative images. Scale bar represents 100 µm. Bottom: quantified results. Error bars represent mean ± SEM (n=6). Data are representative of two independent experiments. ** indicates $p < 0.01$, and **** indicates $p < 0.0001$ (one-way ANOVA test). **E.** HSCs transduced with control virus or virus containing the cDNA encoding dominant negative mutant FYN (FYN-DN) were treated with DMSO or 100 nM NCMC for 48 hours. Expression of *COL1A1* was quantified by qPCR. Error bars represent mean ± SEM (n=3). Data are representative of three independent experiments). ns indicates not significant ($p > 0.05$), * indicates $p < 0.05$, ** indicates $p < 0.01$, and **** indicates $p < 0.0001$ (two-way ANOVA test). **F.** Phospho-ERK and phospho-FAK levels were determined by Western blot in control HSCs and HSCs overexpressing DN-FYN. Left: representative Western blot results. Right: quantified results. Representative of two independent experiments. This figure has four supplements.

42
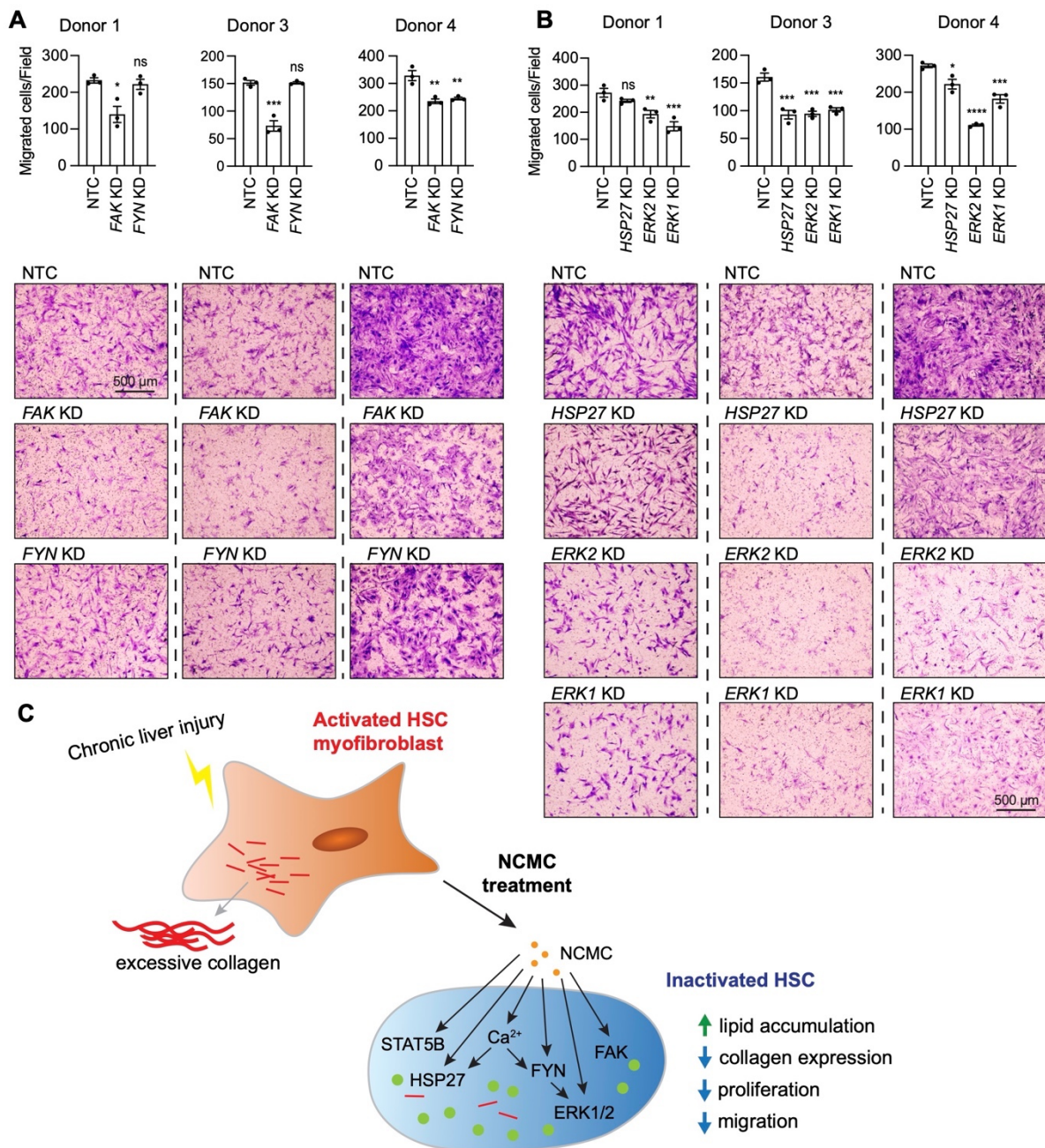
Figure 7. ERK and FAK regulate HSC migration

A-B. Kinases were depleted in HSCs with pooled siRNAs. NTC indicates non-targeting siRNA control. KD indicates the gene transcript that is knocked down. After 72 hours, cells were seeded for transwell migration assay. Migration was assayed at 24 hours for HSCs from donor 1 and 4, and 6 hours for HSCs from donor 3. Top: quantified results. Error bars represent mean ± SEM (n=3). Results are shown for three donor lines. ns indicates not significant ($p > 0.05$), * indicates $p < 0.05$, ** indicates $p < 0.01$, *** indicates $p < 0.001$, and **** indicates $p < 0.0001$ (one-way ANOVA test). Bottom: representative images. Scale bar represents 500 µm. **C.** Schematic summarizing the signaling pathways triggered by NCMC treatment and the effect on HSC activity. Red lines represent collagen, orange spots represent NCMC, and green spots represent lipid droplets.

43

1200   **Table 1. Candidates from small molecule screening**

Compound Name	DRC Score	Known function
Cyproheptadine *	1.0	serotonin antagonist and antihistamine
Emetine *	1.0	anti-protozoal, inhibitor of Zika and Ebola viruses
Homoharringtonine *	1.0	translation elongation inhibitor
Nanchangmycin *	1.0	polyether ionophore antibiotic, inhibitor of Zika virus
Ouabain *	1.3	Na/K-ATPase inhibitor
Digitoxigenin *	1.7	Na/K-ATPase inhibitor
Digoxin *	1.7	Na/K-ATPase inhibitor
Trichostatin A *	1.7	histone deacetylase inhibitor
AT7867, HMSL10154-101-1	1.8	multi-kinase inhibitor
PCI-24781 (Abexinostat) *	2.0	histone deacetylase inhibitor
Dasatinib	2.0	multi-kinase inhibitor
ChemBridge 35093961	2.3	IKK inhibitor
Homochlorcyclizine dihydrochloride	2.3	antihistamine
LY2608204	2.3	glucokinase activator
Vandetanib	2.3	multi-kinase inhibitor
BIX01294 (hydrochloride hydrate)	2.7	G9a histone methyltransferase inhibitor
HMSL10378-101	2.7	predicted to target GSK3B at 1 nM (ChEMBL)
Crizotinib	2.8	multi-kinase inhibitor
Solifenacin succinate	3.0	muscarinic receptor antagonist

1201

1202   * Compounds with an EC50 less than 5 µM.
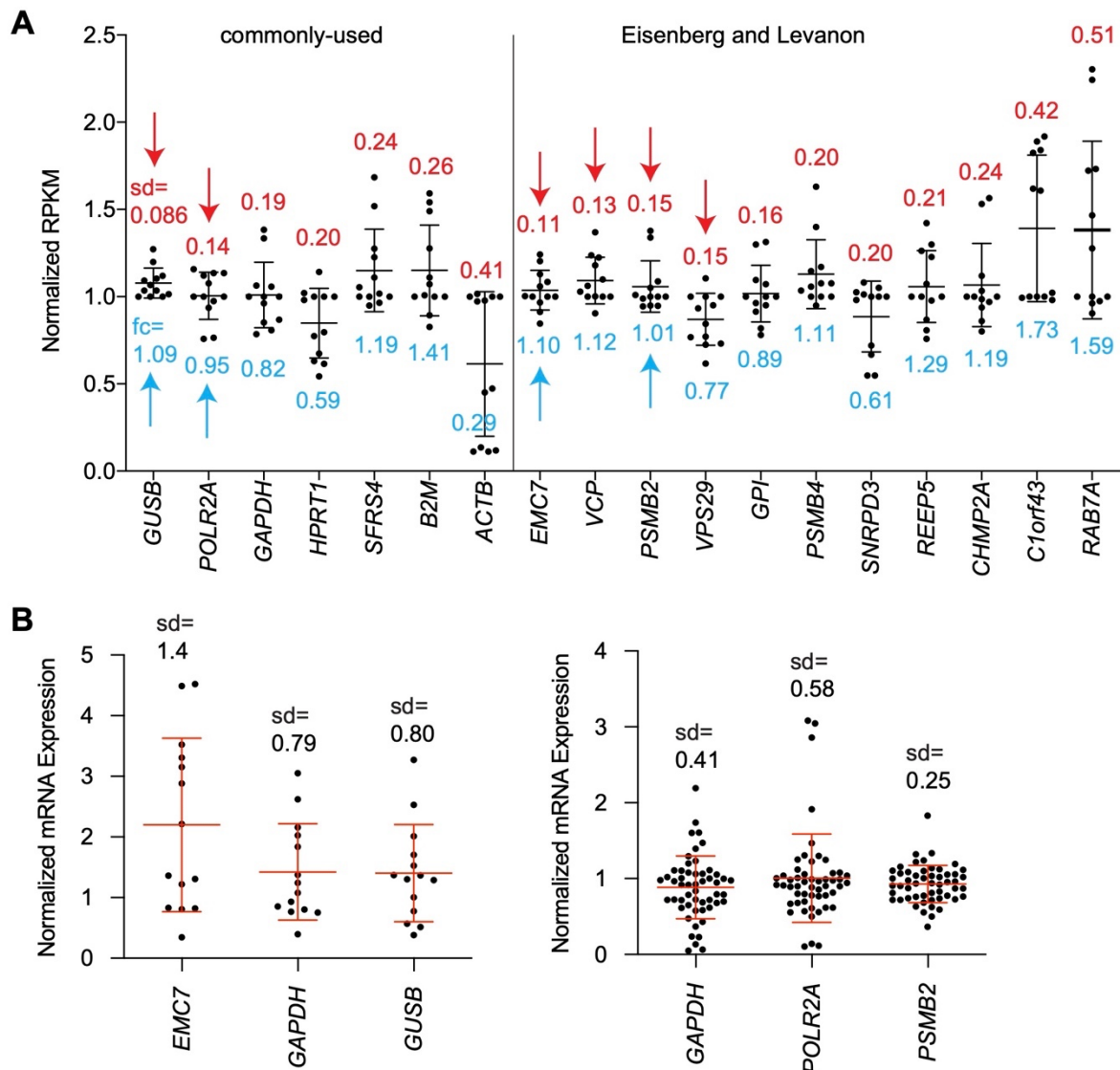
44

Figure 1 – figure supplement 1. Selection of *PSMB2* as the reference mRNA for the qPCR-based secondary screening assay

A. Expression of house-keeping genes in HSCs was plotted by RPKM as previously quantified (Chen et al., 2017). Three pairs of samples were used in this analysis: ceramide treatment vs control, nortriptyline treatment vs control, nortriptyline treatment vs control in TGF-β treated HSCs (Chen et al., 2017). Each dot represents the result from one sample, and bars represent mean ± standard deviation (sd). The value of sd is indicated above each mRNA. The fold change (fc) of *EMC7*, *VCP*, *PSMB2* and *VPS29* in inactivated HSCs (ceramide or nortriptyline-treated) compared to corresponding control groups is indicated below the dots. Two groups of reference mRNAs were analyzed -- commonly used ones (left) and genes that are expressed uniformly across tissues (Eisenberg & Levanon, 2013). Red arrows indicate samples with sd of 0.15 or less. Blue arrows highlight the reference mRNAs with fold change of no more than 10% in inactivated HSCs and were selected for further analysis. *GAPDH*, which is used routinely as a reference control was also included. **B.** Quantification of expression of *EMC7*, *GAPDH*, *GUSB*, *POLR2A*, and *PSMB2* from HSC cDNA samples (left: n=14, right: n=53) that were reverse transcribed from equal amounts of total input RNA. All samples were normalized to the mean value of its own control group before they were combined for each of the reference mRNAs. Each dot represents the result from one sample, and bars represent mean ± standard deviation (sd) of all the tested samples. The value of sd is indicated above each mRNA.
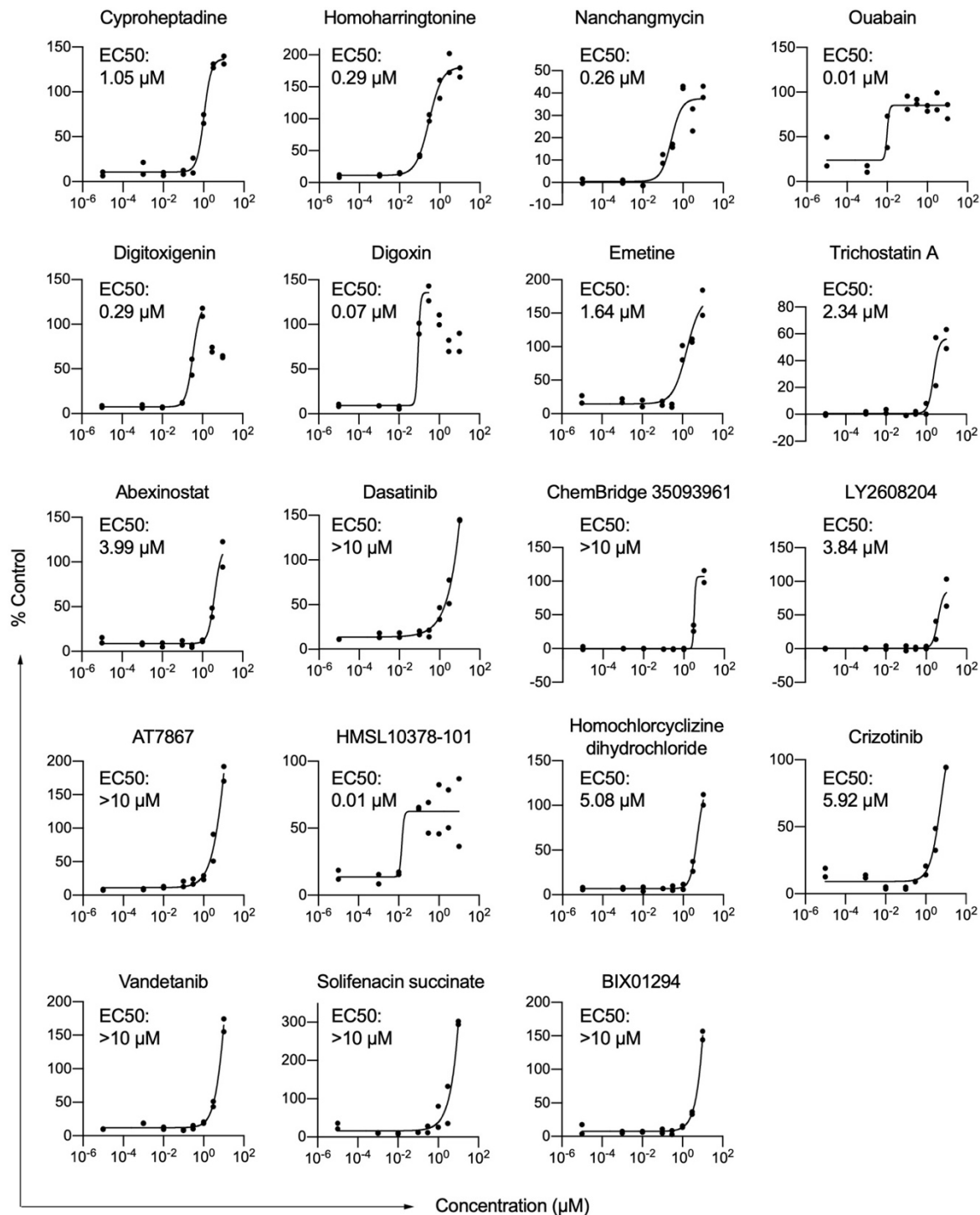
Figure 1 – figure supplement 2. Nineteen compounds were identified to induce lipid accumulation in HSCs.

HSCs from human donor 2 were treated with compounds at indicated concentrations. Each dot represents one well (n=2 technical replicates per concentration). Curves were generated by fitting the data into a sigmoidal equation. For digitoxigenin and digoxin, the highest two or three concentrations respectively were not used for fitting the curves due to the toxicity at these concentrations. If a compound was tested more than one time, only one representative curve is shown here, while the average score from all curves was used for ranking the compounds. Results from each individual experiment and data from all replicates are in Supplementary Table 6.

46
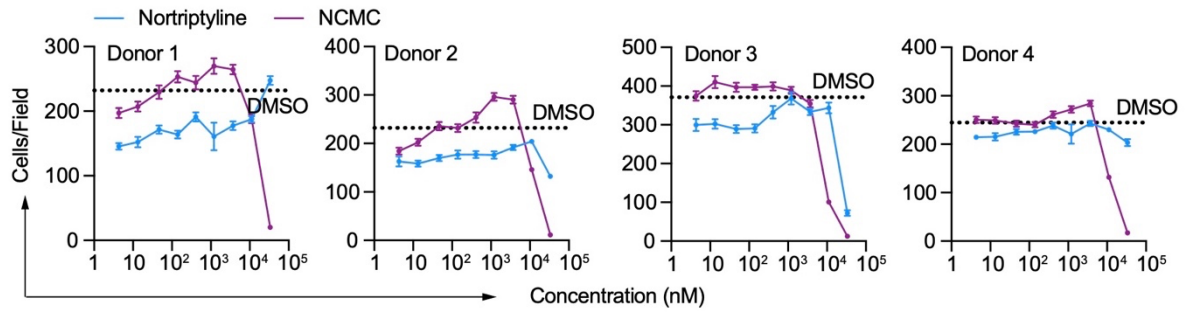
Figure 2 – figure supplement 1. Effect of NCMC on cell number

Effects of NCMC (purple) and nortriptyline (blue) on cell numbers in HSCs isolated from four different human donors at 48 hours. Dotted line represents the mean number of cells per microscopic field in DMSO control wells. Error bars represent mean ± SEM (n=12). One experiment was performed in each of the four donors.
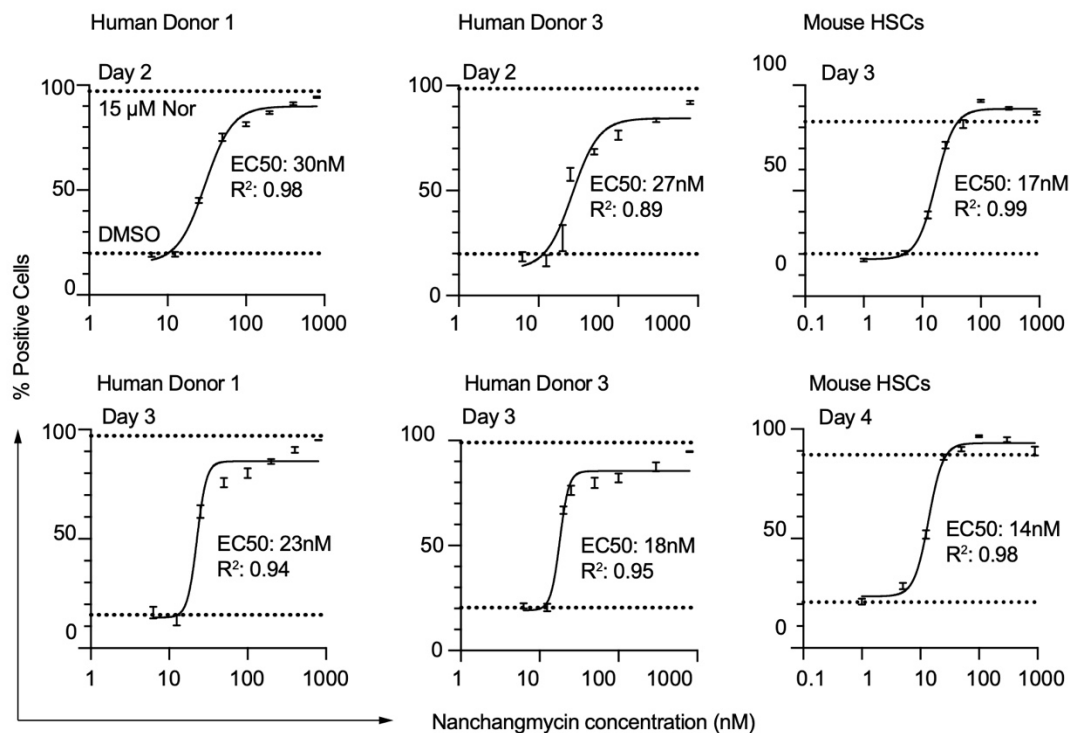
Figure 2 – figure supplement 2. Dose response curves of NCMC treatment at different time points in HSCs.

HSCs isolated from human donor 1 (left two panels), human donor 3 (middle two panels) and mouse (right two panels) were used. Dotted line represents the mean percentage of Bodipy-positive cells in DMSO negative control wells (lower) or nortriptyline positive control wells (upper). Error bars represent mean ± SEM (n=6). EC50 and R^2 are shown.

1249
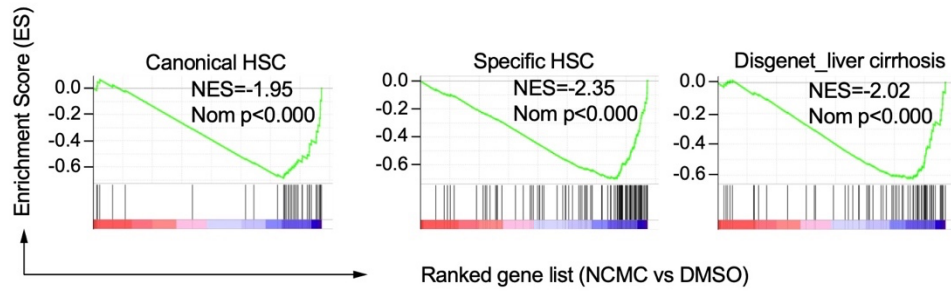
Figure 3 – figure supplement 1. Gene set enrichment analysis results of HSC (Zhang et al., 2016) and cirrhosis (Piñero et al., 2020) gene signatures
NES refers to Normalized Enrichment Score. Nom P refers to Nominal P value. Vertical black lines refer to the gene hits in the indicated signatures. Red color indicates positively correlated, and blue color indicates negatively correlated.
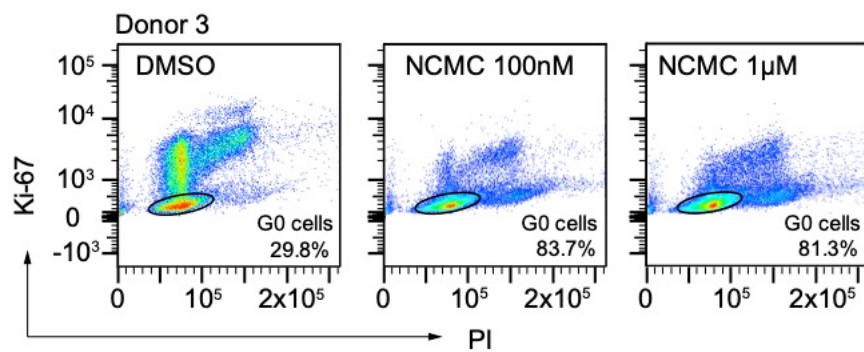
Figure 4 – figure supplement 1. Flow cytometry analysis of Ki-67 and PI stained HSCs
HSCs from human donor 3 were treated with DMSO or nanchangmycin (NCMC) for 24 hours
prior to flow cytometry analysis with Ki-67 and PI. Plots are representative of two independent
experiments.
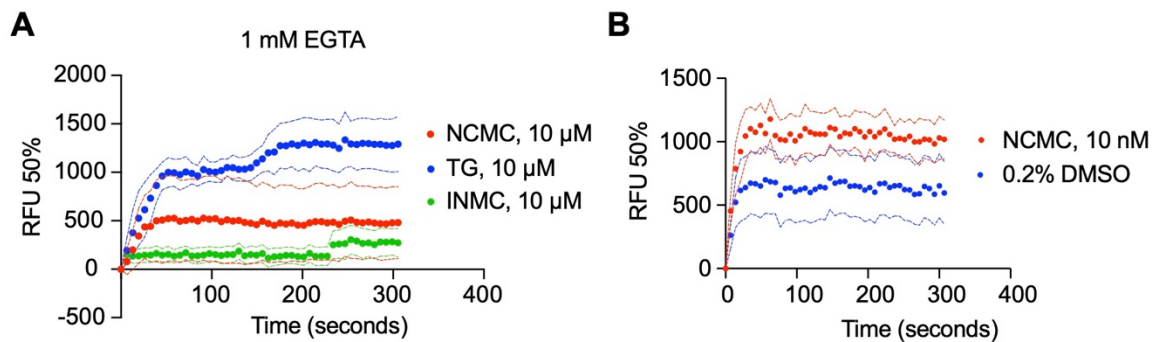
Figure 4 – figure supplement 2. Measurement of cytosolic calcium level using fluo-4 NW

A. HSCs from donor 3 were pre-loaded with fluo-4 NW and fluorescent intensity was read immediately after adding compounds in the presence of 1 mM EGTA (NCMC: nanchangmycin (red), TG: thapsigargin (blue), INMC: ionomycin (green)). The plot demonstrates results from three independent experiments. Solid dots represent mean, and dotted lines represent SEM (n=3). RFU: Relative fluorescence unit. **B.** HSCs from donor 3 were pre-loaded with fluo-4 NW and fluorescent intensity was read immediately after adding 0.2% DMSO or 10 nM NCMC dissolved in DMSO (without EGTA). The plot demonstrates results from three independent experiments. Solid dots represent mean, and dotted lines represent SEM (n=8 for DMSO, n=4 for NCMC). DMSO at 0.2% was selected as a negative control, as this was the highest concentration of DMSO to which HSCs were exposed, as a solvent. NCMC, TG and INMC were all dissolved in DMSO.
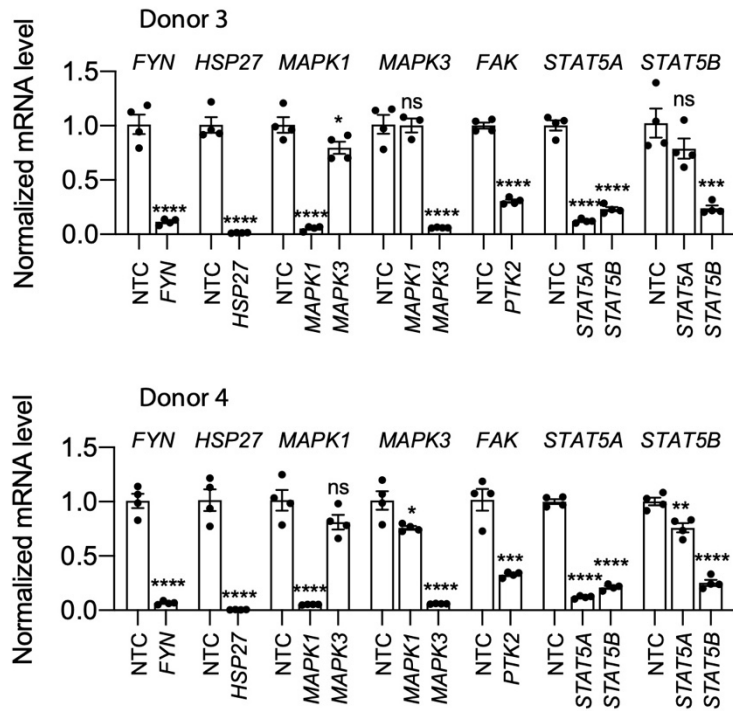
Figure 5 – figure supplement 1. Knockdown efficiency of each siRNA pool in HSCs from human donor #3 (top) and donor #4 (bottom) compared to a non-targeting siRNA control (NTC)

Error bars represent mean ± SEM (n=4). One experiment was performed for each donor shown. ns indicates not significant ($p > 0.05$), * indicates $p < 0.05$, ** indicates $p < 0.01$, *** indicates $p < 0.001$, and **** indicates $p < 0.0001$ (one-way ANOVA test).
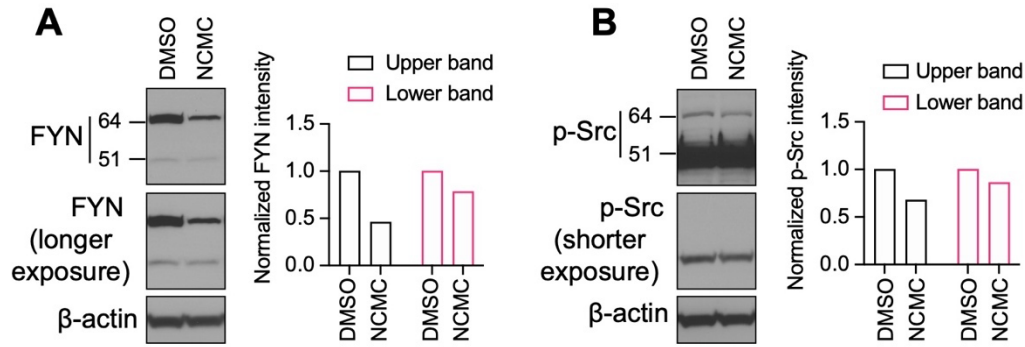
Figure 6 – figure supplement 1. Western blot of HSCs treated with 1µM NCMC for 18 hours

The same samples were loaded for A and B on the same gel. The membrane was cut and incubated with FYN and p-Src family antibodies separately. Bands were detected for FYN at 64 kilodaltons (kD) (Upper band) and 51 kD (Lower band). Two different exposure times are shown for FYN in (A) and p-Src (B) to evaluate both bands. β-actin is used as a loading control. (Data are representative of three independent experiments).
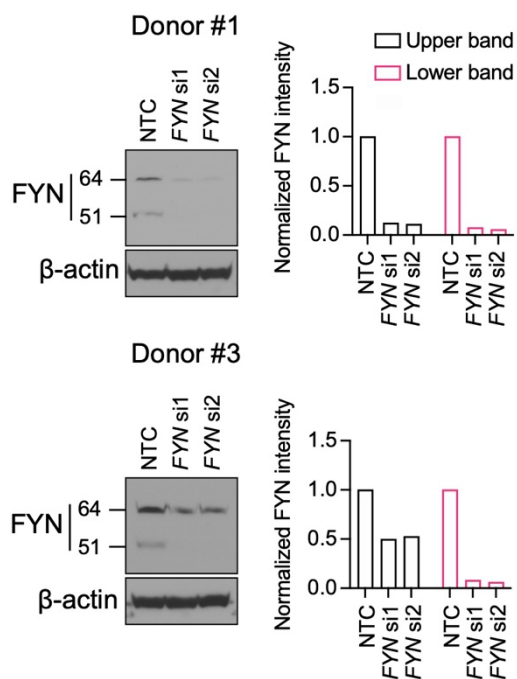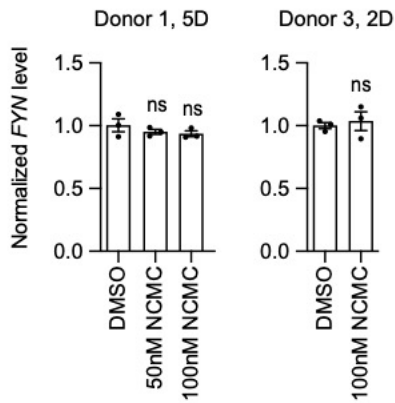
1292

Figure 6 – figure supplement 2. Western blot for FYN
HSCs were transfected with siRNAs targeting *FYN* (si1 and si2) and a non-targeting siRNA control (NTC). Western blot was performed on day 3 (representative of two independent experiments).

1298

Figure 6 – figure supplement 3. *FYN* mRNA level was not affected by NCMC treatment
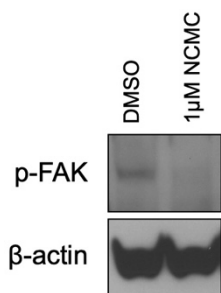HSCs were treated with NCMC for indicated number of days (D). *FYN* level was analyzed by qPCR. Error bars represent mean ± SEM (n=3). Data are representative of two independent experiments. ns indicates not significant (p > 0.05) by one-way ANOVA for donor 1 and Student's t-test for donor 3.

1305

Figure 6 – figure supplement 4. NCMC decreases FAK phosphorylation
Western blot of HSCs treated with DMSO control or 1 μM NCMC for 18 hours. β-actin is used as a loading control (representative of three experiments).

1310 **List of supplementary tables**

1311 Supplementary Table 1_Small-molecule Compound Libraries

1312 Supplementary Table 2_Primary Screen Results

1313 Supplementary Table 3_711 Hits from Primary Screen

1314 Supplementary Table 4_Clustering of Primary Screen Candidates

1315 Supplementary Table 5_Secondary Screen Results

1316 Supplementary Table 6_DRC Screen Results

1317 Supplementary Table 7_GSEA of Ontology Gene Sets

1318 Supplementary Table 8_HSC and Liver Cirrhosis Gene Signatures

1319